The Impact of Horizontal Grid Spacing on the Microphysical and Kinematic Structures of Strong Tropical Cyclones Simulated with the WRF-ARW Model

ALEXANDRE O. FIERRO, ROBERT F. ROGERS, AND FRANK D. MARKS

NOAA/Hurricane Research Division, Atlantic Oceanographic Meteorological Laboratory, Miami, Florida

DAVID S. NOLAN

Rosenstiel School of Marine and Atmospheric Science, University of Miami, Miami, Florida

ABSTRACT

Using the Advanced Weather Research and Forecasting numerical model, the impact of horizontal grid spacing on the microphysical and kinematic structure of a numerically simulated tropical cyclone (TC), and their relationship to storm intensity was investigated with a set of five numerical simulations using input data for the case of Hurricane Rita (2005). The horizontal grid spacing of the parent domain was systematically changed such that the horizontal grid spacing of the inner nest varied from 1 to 5 km by an increment of 1 km, this while keeping geographical dimensions of the domains identical.

Within this small range of horizontal grid spacing, the morphology of the simulated storms and the evolution of the kinematic and microphysics field showed noteworthy differences. As grid spacing increased, the model produced a wider, more tilted eyewall, a larger radius of maximum winds, and higher-amplitude, low wavenumber eyewall asymmetries. The coarser-resolution simulations also produced larger volume, areal coverage, and mass flux of updraft speeds ≥ 5 m s^{-1}; larger volumes of condensate and ice-phase particles aloft; larger boundary layer kinetic energy; and a stronger secondary circulation. While the contribution of updrafts ≥ 5 m s^{-1} to the total updraft mass flux varied little between the five cases, the contribution of downdrafts ≤ -2 m s^{-1} to the total downdraft mass flux was by far the largest in the finest-resolution simulation.

Despite these structural differences, all of the simulations produced storms of similar intensity, as measured by peak 10-m wind speed and minimum surface pressure, suggesting that features in the higher-resolution simulations that tend to weaken TCs (i.e., smaller area of high surface fluxes and weaker total updraft mass flux) compensate for features that favor TC intensity (i.e., smaller-amplitude eyewall asymmetries and larger radial gradients). This raises the possibility that resolution increases in this range may not be as important as other model features (e.g., physical parameterization and initial condition improvements) for improving TC intensity forecasts.

1. Introduction

Timely and accurate forecasts of tropical cyclones (TCs) represent one of the major challenges in the meteorological modeling community. Inaccurate forecasts can lower the confidence of the public and result in the waste of millions of dollars during mass evacuations. In the last two decades, modeling and observational studies of TCs (e.g., Willoughby et al. 1982; Emanuel 1986, 1988; Willoughby 1990a,b, 1998; Powell 1990a,b; Gray 1995;

Shapiro and Franklin 1999; Braun and Tao 2000; Wang 2002a; Zhu and Smith 2002; McFarquhar and Black 2004; Zhu and Zhang, 2006; Rogers et al. 2007) have led to significant improvement of our knowledge of TCs. However, until now, very few studies have focused their attention on the impact of grid spacing in general and particularly, on the impact on TC structure and intensity.

The first comprehensive study on the effect of coarse (12 km) to cloud-resolving (1 km) horizontal grid spacing was carried out by Weisman et al. (1997). In their simulations of continental squall lines, significant differences were simulated in the mesoscale circulation and convective structure as horizontal resolution varied. In particular, the coarser cases exhibited significant delay in the

Corresponding author address: Alexandre O. Fierro, AOML/HRD, 4301 Rickenbacker Causeway, Miami, FL 33149.
E-mail: alexandre.fierro@noaa.gov

onset of convection, which once formed tended to produce an overestimate of the vertical mass transport. This was because the coarser grid spacing cases were not able to reproduce nonhydrostatic effects properly. In a similar study, Bryan and Rotunno (2005) and Bryan (2006) found that for horizontal grid spacing ranging between $\Delta x = \Delta y = 125$ m and 8 km, his model produced on average the largest updraft speeds for Δx, Δy between about 500 m and 1 km and also produced the largest upward mass fluxes for Δx, Δy values between 1 and 2 km. Indeed, at finer horizontal resolution (i.e., <500 m), the majority of the simulated updrafts are smaller and hence, more prone to dilution by entrainment.

The motivation for our work arose from recent studies comparing TC microphysics fields from high-resolution numerical simulations with airborne Doppler vertical motion and reflectivity measurements (McFarquhar et al. 2006; Rogers et al. 2007, hereafter R07). Both of these studies found discrepancies between simulated and observed kinematic and microphysical distributions. For instance, R07 found in their fifth-generation Pennsylvania State University–National Center of Atmospheric Research (PSU–NCAR) Mesoscale Model (MM5) simulations of Hurricanes Bonnie (1998) and Floyd (1999) that the distribution of eyewall vertical velocity narrowed with height, in contrast with airborne Doppler observations (Black et al. 1996). Both modeling studies did find a pronounced high bias in reflectivity, while R07 also found that the simulations failed to produce the sharp decrease in reflectivity with height normally seen in radar measurements (Black et al. 1996). They hypothesized that horizontal resolution could play a role, among many other factors, in explaining those discrepancies. However, until now, no modeling studies have evaluated in detail the impacts of horizontal ($\Delta x = \Delta y$) grid spacing on the simulated microphysical and kinematic fields in TCs, and in turn how those fields are related to storm intensity. This problem is important because many studies on convection organized on the mesoscale (including TCs) systematically make use of horizontal grid spacing of less than 10 km within the innermost mesh. Also, the future of real-time hurricane forecasts using mesoscale models will increasingly make use of cloud-resolving grid spacing (i.e., Δx, $\Delta y < 5$ km) as computer power increases. As operational models increase in horizontal (and vertical) resolution, the need for a systematic testing of the impact of resolution on the simulated storm's microphysics and kinematics, and in turn how the latter modulates TC intensity, has become more important. The results obtained herein could have potential applications to widely used research and forecast models such as MM5, the Advanced Research Weather Research and Forecasting

TABLE 1. Dimensions of the domains for the five cases tested herein.

Cases (outer/inner)	Nx (outer)	Ny (outer)	Nx (inner)	Ny (inner)
15–5 km	159	75	84	84
12–4 km	200	93	105	105
9–3 km	266	124	139	139
6–2 km	399	186	211	211
3–1 km	797	373	421	421

(WRF-ARW) model, the Hurricane WRF (HWRF), or the Geophysical Fluid Dynamics Laboratory Hurricane Prediction system (GFDL-HPS).

2. Model description and initialization procedures

The model used for this study was the WRF-ARW dynamical core (version 2.2; Skamarock et al. 2005). The WRF-ARW 2.2 solves the fully compressible nonhydrostatic Euler equations of motion in flux form on a Cartesian Arakawa C grid with terrain-following sigma coordinates. The choices made in the physics and dynamical set up are the following: the turbulent fluxes are parameterized using the downgradient K-theory. The parameterization of turbulence in the boundary layer (BL) selected is the Eta implementation of the 1.5-order closure of Mellor and Yamada (1982) by Janjic (1994).

In this work, an original approach has been devised to study the impact of horizontal resolution in a nested domain configuration: While the parent and nested domains were fixed to cover the same geographical area, the horizontal grid spacing of the parent (i.e., outer) domain was systematically varied such that the horizontal grid spacing of the inner nest ranged between 1 and 5 km by increments of 1 km. In other words, our study consists of a set of five numerical simulations, referred to as the 15–5-, 12–4-, 9–3-, 6–2-, and 3–1-km cases, respectively, whose domains all cover the same area for consistency (Fig. 1) rounded to the nearest grid point (Table 1). Furthermore, all simulations used identical model settings and input data and were all performed on 64 processors.

The simulation domain is centered at latitude = 24.94°N and at longitude = 84.74°W with horizontal dimensions of $X \times Y \times Z = 2400$ km $\times 1150$ km $\times 20.3$ km (Fig. 1). A two-way interactive vortex-following inner nest (Michalakes et al. 2005) with a parent domain aspect ratio 1:3 having dimensions of $X \times Y \times Z = 420$ km $\times 420$ km $\times 20.3$ km was placed in the parent domain. The inner nest's size was determined such that it covers most of the simulated storm (eyewall and main rainbands) at all times. All cases used a stretched vertical grid in the BL and the upper troposphere with
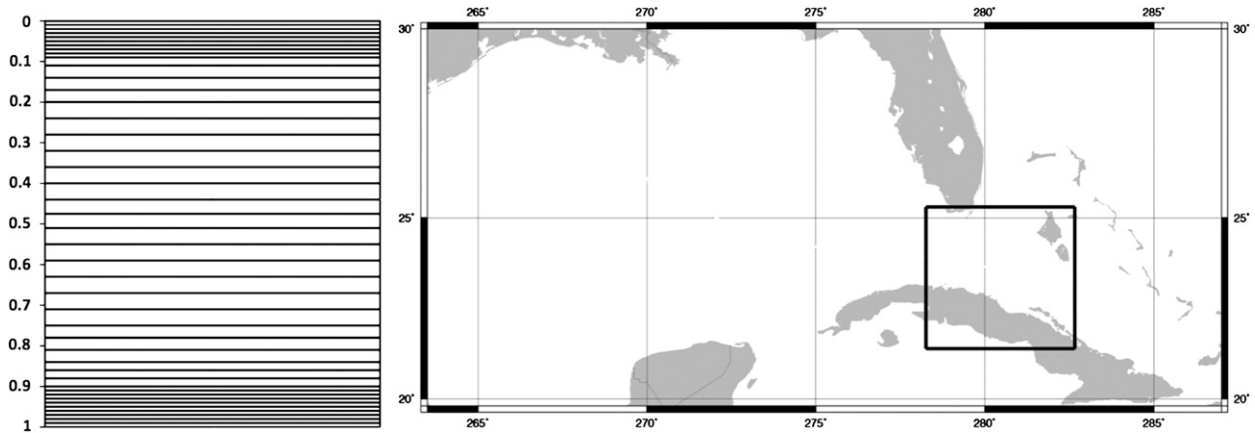
FIG. 1. Sketch of the distribution of the sigma levels and simulation domains selected for all the simulations in this study. The inner moving nest, where all our analysis is focused, is shown by the black square.

43 levels (Fig. 1). Based on MM5 simulations, this particular vertical grid configuration in Fig. 1 ensures a better representation of these two regions of the atmosphere (Dougherty and Kimball 2006), which have been shown to be critical for TCs: The air–sea surface flux exchanges of moist enthalpy via surface latent heat and sensible heat fluxes, which are the primary source of energy of the TC (e.g., Emanuel 1986), occur in the BL, while the strength of the secondary circulation heavily relies on an uninterrupted anticyclonic ventilation flow in the upper troposphere (near 15–18 km). It would also be relevant in future hurricane modeling studies to evaluate the sensitivity to vertical grid spacing.

The WRF-ARW 2.2 model features several bulk microphysics schemes to choose from. Most are essentially based on the work from Lin et al. (1983) and Rutledge and Hobbs (1983, 1984). The present study will make use of the hybrid (double moment for ice crystals and single moment for all other species) Thompson et al. (2004) scheme. Preliminary sensitivity testing with other schemes containing graupel as a species such as the WRF single-moment 6-class microphysics (WSM6) scheme (Hong et al. 2004) revealed that the graupel mixing ratios commonly exceeded 6 g kg^{-1} in the eyewall of the simulated TC, which is an unrealistically large amount based on in situ observations (Black and Hallett 1986, 1999). In the Thompson scheme, riming growth of snow is required to exceed depositional growth of snow by a factor of 3 before rimed snow transfers into the graupel category, resulting in more realistic values for graupel mixing ratio in the eyewall. Other schemes such as the WSM5 (Hong et al. 2004) or Kessler (1969) were not selected simply because they did not incorporate enough hydrometeor species for our study, particularly graupel, which is almost always associated with strong convection ($\geq$10 m s^{-1}, e.g., McFarquhar et al. 2006). Black

and Hallett (1986) showed that most of the cloud volume in the hurricane core was composed of ice crystals and snow aggregates. Therefore, the ability to predict ice number concentration with the Thompson scheme is desirable. The densities of snow and graupel were set to 100 and 400 and g kg^{-1}, respectively, based on observed values (Black 1990).

Several preliminary tests with the cumulus parameterization scheme (CPS) turned off in the parent domain resulted in a delay (which not surprisingly increased as Δx, Δy increased) of the storm formation and in some cases (particularly when Δx, $\Delta y > 5$ km) caused the storm to fail to develop. Therefore, in the outer domain, the Kain–Fritsch scheme (1993) was used in all our cases (see later in the section) for consistency, while in the inner nest no CPS was used. For the finest-resolution case presented herein, namely 3–1 km, a cumulus scheme in the outer nest is not required as at $\Delta x = \Delta y = 3$ km, large clouds are explicitly resolved, and also because CPS schemes are in essence not designed to be used at horizontal and vertical grid spacings smaller than about 5–10 km (Molinari and Dudek 1992). In this study, however, we wish to put emphasis on the need to keep *consistency* between all cases. Also, the analysis presented herein *entirely* focuses on the inner-nest data, whose dimensions were chosen to cover the great majority of the storm's convection at all times in all five cases. Results from an additional simulation of the 3–1-km case with CPS turned off in the outer domain revealed that the simulated storm intensity and structure were overall similar (not shown). The minimum surface pressure and maximum 10-m surface wind speed followed almost the exact same evolution while being about 5 hPa higher and within 4 m s^{-1}, respectively. There was also little difference (within 50 miles) in the simulated tracks at and after 12 h of simulation time.
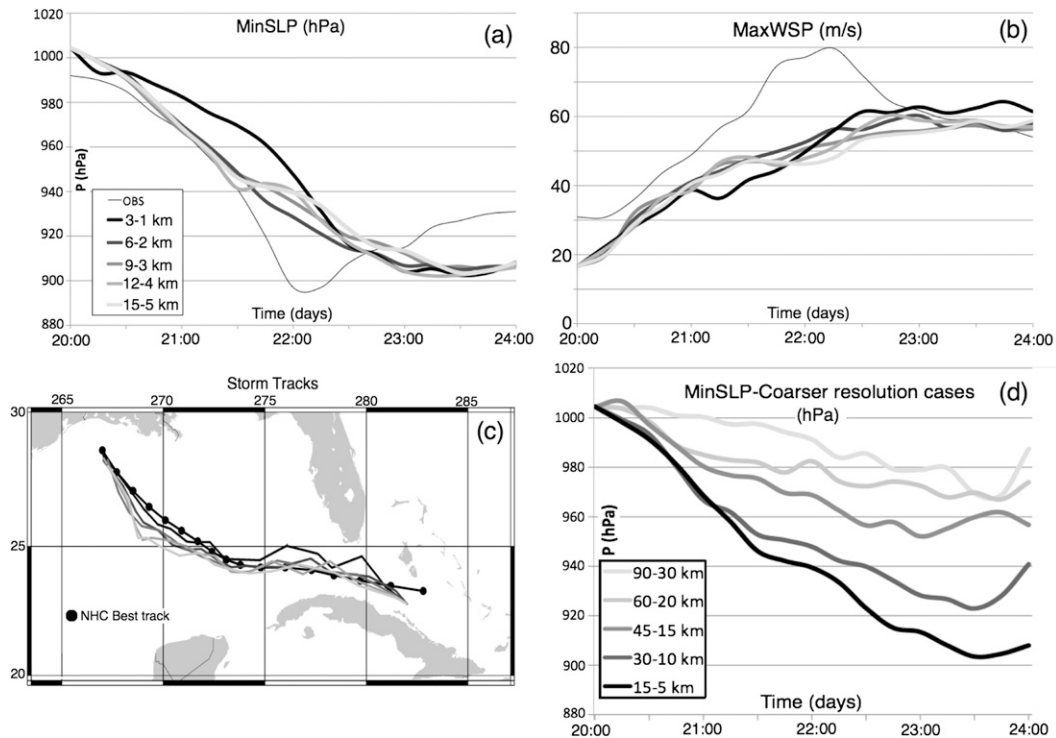
FIG. 2. Time series of (a) min SLP (mb) and (b) maximum 10-m wind speed (m s^{-1}) for the five cases shown in Table 1 overlaid with the National Hurricane Center (NHC) best track (thin black line). (c) The storm tracks for those five cases overlaid with the best track labeled with black disks. (d) As in (b), but for four extra simulations carried out at coarser resolution with the 15–5-km case shown in the thick black line for reference. The legends for (a),(b), and (c) are shown in the lower-left corner of (a). Similarly, the legend for (d) is shown in the bottom-left corner.

The initial and boundary conditions (updated every 6 h) were obtained by preprocessing the National Centers for Environmental Prediction (NCEP) aviation (AVN) final analyses. The simulation was started at 0000 UTC 20 September 2005, when Rita was still a category 1 hurricane on the Saffir–Simpson scale (Simpson 1974), and ended at 0000 UTC 24 September 2005 just before the storm made landfall. The inner nest was placed in the domain only 6 h after the initial time at 0600 UTC 20 September 2005. Several preliminary tests revealed that this timing of domain initiation was optimal and guaranteed a strong mature hurricane.

It is important to point out that, in the current study, it is *not* necessary to precisely reproduce Rita (2005) in terms of intensity and track evolution. However, it is important that in all our cases the simulated TCs follow a similar track (see below). Our study focuses on questions that are more general and case independent and therefore could be applied to any strong major hurricane simulation with a similar model (e.g., MM5 and HWRF). As shown by Davis et al. (2008), this was a difficult case to simulate, because this TC experienced rapid intensification (RI; as much as 40 hPa in 12 h;

Fig. 2a) followed by a rapid rise in minimum surface central pressure due to an eyewall replacement cycle and increasing vertical shear and lower-tropospheric dry air (Knabb et al. 2005). After a rather extensive set of sensitivity tests of the physics options (including microphysics, radiation, CPS, BL, domain timing, base-state temperature, boundary, and initial conditions from different input data sources) without any data assimilation, the model was still not able to capture the intensity evolution of this storm over the ocean. Moreover, despite showing some improvement in intensity prediction for this case, recent results using data assimilation via the ensemble Kalman filter (EnKF; Zhang et al. 2009) method of airborne Doppler tangential winds from the National Oceanic and Atmospheric Administration (NOAA) P-3 tail radar did not succeed in capturing the intensity evolution of Rita over the ocean (F. Zhang 2008, personal communication). Furthermore, although it is possible to reproduce an eyewall replacement cycle with WRF or MM5 (e.g., Houze et al. 2007) it is only on rare occasions that the model will be able to simulate this storm-scale event at the right time. Despite those challenges, by using input boundary conditions derived

TABLE 2. The first two columns show the inflow in and vertical mass fluxes (kg m s^{-1}) out of a cylinder of radius of 60 km and height of 1.1 km MSL from the storm's center (defined as the minimum surface pressure). The third column on the right shows the BL integrated kinetic energy within a cylinder of height 1.1-km MSL and a radius of 120 km from the storm's center. Inflow and outflow matches within 10% because those were computed from interpolated axisymmetric fields and also because radial inflow used height, not pressure (mass) coordinates.

Cases	Inflow mass flux ($\times10^9$ kg m s^{-1})	Vertical mass flux ($\times10^9$ kg m s^{-1})	BL kinetic energy ($\times10^8$ m^2 s^{-2})
90–30 km		Storm center ill defined	
60–20 km	−2.27	2.94	2.731
45–15 km	−2.12	3.5	3.993
30–10 km	−6.31	8.19	7.642
15–5 km	−9.153	10.15	10.938
12–4 km	−9.18	10.55	11.900
9–3 km	−7.324	7.871	8.938
6–2 km	−4.683	5.146	8.141
3–1 km	−5.749	6.253	6.888

from global model analyses every 6 h (i.e., simulation mode), WRF-ARW was able to capture the track of Rita well in all the cases presented herein (Fig. 2c), therefore guaranteeing that the simulated storms in all five cases are experiencing similar environmental conditions. This is not a surprising result as Marks and Shay (1998) showed that, unlike intensity, track prediction depends more on large-scale processes that can be resolved with coarse grid prediction models (Goerss 2006). This allows an examination of the sensitivity of simulated TC microphysics structure and kinematics to horizontal grid spacing in an environment similar to that of Hurricane Rita. The analysis will focus on the intensification period (section 3a), and the later, steady-state stage of the storm (section 3b).

3. Results

a. Evolution of the simulated storm's intensity

Except for the finest-resolution case (3–1 km; Table 1), the other four simulated storms underwent a remarkably similar intensity evolution in terms of maximum 10-m wind speed (maxWSP) and minimum sea level pressure (minSLP; Figs. 2a,b). In their WRF-ARW simulation of Hurricane Katrina (2005), Davis et al. (2008) found, on the other hand, that minSLP and maxWSP did show nonnegligible changes as Δx, Δy were decreased from 4 to 1.3 km (by as much as 20 hPa and 13 m s^{-1}, respectively) while almost no difference was observed between 12 and 4 km. In this simulation, the 3–1-km case remained weaker for the first 36 h, after which point the intensification rate was greater than the other four storms. The fastest drop in minSLP, also coincident with the largest increase in maxWSP, was observed for the 3–1-km case, with a maximum drop of 35 hPa in 12 h and a 12 m s^{-1} maxWSP increase in 12 h

(Figs. 2a,b). For *all* cases, the simulated minSLP reached a steady-state value near 905 hPa after 0600 UTC 23 September 2005 while the maxWSP reached a steady-state value near 57 m s^{-1} except for the 3–1-km case, which produced a higher maxWSP value of 62 m s^{-1}. This behavior naturally raises the following questions: while these cases underwent a relatively similar intensity evolution, will there be any significant differences in the microphysics, kinematics, and storm structure? How are any structural differences related to the intensity of the simulated storm?

In the light of the above results, it would be relevant to determine at what coarser horizontal resolution the storm intensity would substantially decrease. Toward this goal, we carried out four additional simulations at coarser resolution following the same philosophy of our five cases shown in Table 1 *for consistency*. Those simulations were labeled 90–30, 60–20, 45–15, and 30–10 km, respectively. The results, not surprisingly, revealed that at as Δx, Δy became greater than 10 km (again focusing on the inner mesh) the storm intensity, BL kinetic energy, updraft mass flux, and inflow mass flux progressively declined (Fig. 2d; Table 2) as inherent storm-scale processes (e.g., R07) and radial gradients were poorly or simply not resolved (not shown). Indeed, Kossin and Eastin (2001) showed that the radial gradient of angular velocity is an important determinant of a tropical cyclone's likelihood of intensification. The tendency for weaker storms at coarser resolution held faithfully (minSLP within 10 mb and maxWSP within 5 m s^{-1}) when the Kain–Fritsch CPS was turned on in the inner mesh. Figure 3 shows that, for 10-km resolution, the peak surface sensible heat fluxes (and moisture flux, not shown) were much weaker than for 5 km by as much as a factor of 3, consistent with weaker BL kinetic energy (Table 2). The latter became even smaller as Δx, Δy increased above 10 km (not shown) as expected from
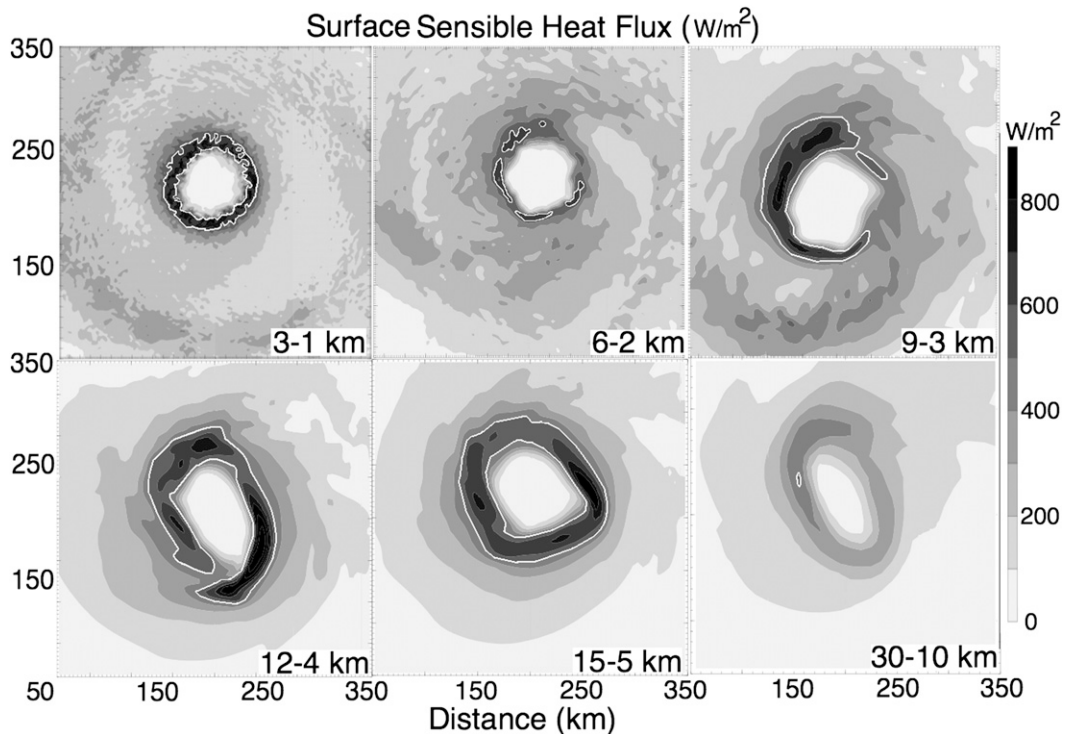
FIG. 3. Horizontal cross sections of surface sensible heat flux at the surface (W m^{-2}) for the five cases shown in Table 1 and for one of the additional simulations shown in Fig. 1d. Legends are shown on the right of the figure. For convenience, the 500 W m^{-2} contour is highlighted by a thick white line.

the even smaller BL kinetic energy (Table 2). It is noteworthy to mention that finer-resolution simulations than our finest-resolution case in Table 1 would also be desirable in the future to determine the relationship between horizontal resolution and intensity at the opposite tail of the resolution spectrum.

b. Kinematic and microphysical structure during steady-state period

In performing the comparisons of storm structure as a function of horizontal resolution, we divided the simulations into two primary time periods: a period of intensification where the storms' minSLP drops from 1000 to 910 hPa in about 2.5 days, and a steady-state period where the minSLP remains nearly constant for 1.5 days afterward. We focus our analysis on the steady-state period here, centered at 0000 UTC 23 September 2005. The lack of intensity variation during this steady-state period allows us to highlight further that, while the simulated storms showed similar minSLP and maxWSP, the morphology, kinematic, and microphysical structure exhibited notable differences. Selecting a single time will also allow for an examination of the spatial structure of the storm in more detail. To ensure that the results were generally consistent during the steady-state period, we compared the fields described in this section over a

12-h period centered at 1200 UTC 23 September 2005. These comparisons revealed no qualitative or quantitative difference with the results presented below.

Single horizontal cross sections were created to provide an initial view of the basic horizontal storm structure (e.g., eye and eyewall size) to determine how those differ despite the small change in intensity of the simulated storms (cf. Figs. 2a,b). The spatial variation of sensible heat flux (Fig. 3) and moisture flux (not shown as it behaved similarly) at the surface shows that as Δx, Δy increased from 1 to 5 km, the areal coverage of larger sensible heat fluxes (i.e., 500 W m^{-2}) also increased. This factor alone would promote the coarser-resolution cases to produce stronger storms (Emanuel 1986). Since this is not the case here (cf. Figs. 2a,b), other factors must be limiting storm intensity in the coarser-resolution cases.

Horizontal cross sections of updraft speeds above the melting level revealed that the two coarsest resolution cases produced the largest updraft speeds (exceeding 12 m s^{-1}; Fig. 4). The simulated updraft magnitudes in our 15–5-km case were much larger than those simulated by Wang (2002a) at $\Delta x = \Delta y = 5$ km, which rarely exceeded 2 m s^{-1} for a simulated storm of similar intensity (minSLP and maxWSP) but much smaller eye diameter (~20 km compared to ~100 km here). Figure 4 and time–height volumes of updrafts ≥5 m s^{-1} (not shown)
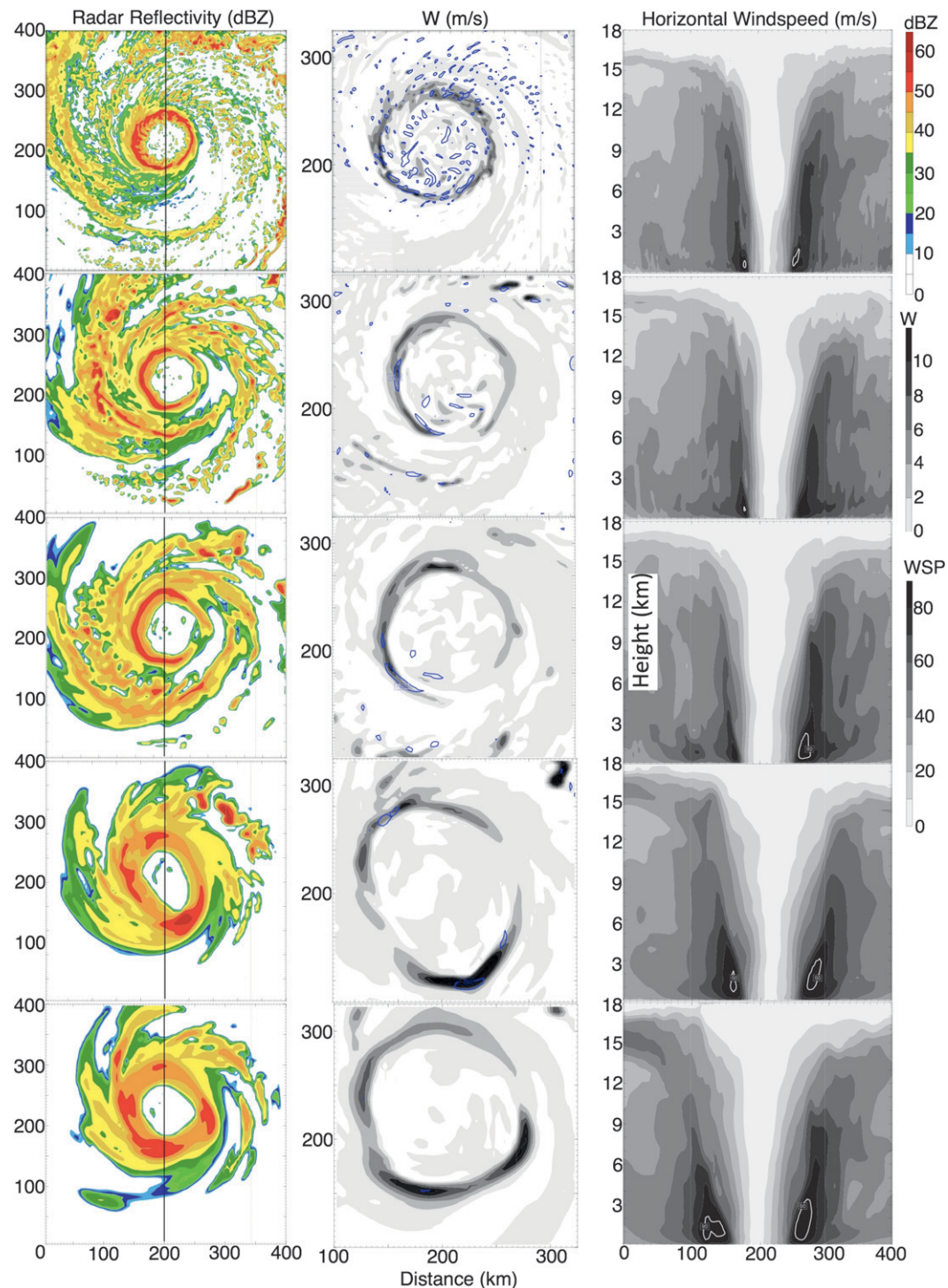
FIG. 4. Horizontal (and vertical) cross sections of radar reflectivity at $z = 1.12$ km (dBZ) and vertical wind (m s^{-1}) at $z = 8$ km at 1200 UTC 23 Sep 2005 for the five cases tested herein. The order of the cases is with the finer-resolution case shown at the top line and the coarsest simulation case shown at the bottom line. The blue contours in the middle column plots show vertical wind speed contours less than or equal to -2 m s^{-1} at $z = 2$ km and the thick white contours in the third column plots show wind speed values of 90 m s^{-1}. The spatial location of the vertical cross sections of the third column are shown by a thick black horizontal line on the horizontal cross sections in the first column. The remaining legends for color and shadings are shown on the right-hand side of the figure.

indicate that the coarser runs had a larger area covered by those moderate updrafts. The finest-resolution case revealed a more complex updraft structure: the eyewall in the finest-resolution cases is composed of numerous smaller updraft entities of about 2–6 m s^{-1} with isolated peaks exceeding 10 m s^{-1}. Those simulated updraft magnitudes are in good agreement with Braun's (2002) 1.3-km MM5 simulation of Hurricane Bob (1991) for a simulated TC of similar intensity (in terms of minSLP and maxWSP). Additional horizontal and vertical cross sections made over a 12-h period centered on 1200 UTC 23 September 2005 (not shown) revealed that in all five cases the maximum updraft speeds rarely exceeded 15 m s^{-1} in the eyewall, which is an encouraging result consistent with observations (Jorgensen et al. 1985; Black et al. 1996). Note the presence of relatively large-amplitude eyewall asymmetries of radar reflectivity in the form of wavenumbers 4 and 2 in the 15–5- and 12–4-km case, respectively (Fig. 4), which have been shown to act as a brake to storm intensity (Peng et al. 1999; Wu and Braun 2004; Yang et al. 2007). It is possible therefore that the gain in intensity by a higher surface heat flux (and therefore BL kinetic energy; Table 2) at coarser resolution shown in Fig. 3 is compensated by an energy loss via large amplitude eyewall asymmetries. The temporal evolution and persistence of these eyewall asymmetries will be analyzed in section 3c.

For the two coarser cases (15–5 and 12–4 km), the eyewalls were wider (Fig. 4). This is a well-known result and has already been documented, for instance, by Yau et al. (2004) in their MM5 simulation of Hurricane Andrew (1992) as Δx, Δy increased from 2 to 6 km. This result was also found by Davis et al. (2008) as Δx, Δy was decreased from 12 to 4 and 1.3 km. Finally, Chen et al. (2007) found the same result in a MM5 simulation of Hurricane Floyd (1999) as Δx, Δy was decreased from 15 to 5 and 1.3 km. The larger eyewalls in the two coarser-resolution cases also produced wider horizontal wind speed contours exceeding 70 m s^{-1}, which as we shall discuss later promote stronger storm surge.

Analyses based on single cross sections are, however, limited because of temporal and spatial variations of the simulated TC's kinematic and microphysics fields. To provide a more general description of the microphysical and kinematic attributes of the storm at that time, radius–height plots of axisymmetric mean quantities during the steady-state period were generated. It is relevant to determine to what extent the simulated vertical structure of averaged fields varies and in turn, how these could further isolate factors favoring/limiting storm intensity in each case. Note that because of the aforementioned larger eyewall asymmetries at coarser resolution, the averages values will be smaller than at finer resolution.

With the exception of the coarsest case (15–5 km), the maximum azimuthal mean of tangential winds (Vt_θ) at 1.12 km exceeded 80 m s^{-1} (Fig. 5). Additionally, the surface wind fields for the two coarser-resolution runs extended farther in radius than the three other cases. As a result, the integrated BL kinetic energy (as defined by Powell and Reinhold 2007) of the simulated storm increased as horizontal resolution decreased (Table 2). It is also worth noting that the eyewall outward slope [defined here as the angle from the vertical of the axis of the radius of maximum wind (RMW) or peak Vt_θ], which here increases as horizontal grid spacing increases, is closely related to the size of the RMW (Stern and Nolan 2009); that is, as the RMW decreases, the slope of the eyewall decreases (i.e., less vertical tilt; Fig. 5). Typical eyewall slopes of radar reflectivity in nonsheared environments observed by radar (Marks 1985) are about 40°–45° from the vertical axis. This is much smaller than the values obtained here for the two coarser-resolution cases, which were about 75° (Fig. 5). However, the finer-resolution cases revealed radar reflectivity slope of about 50°–60°, in closer agreement with observations (Fig. 6). It is important to note that similar to observations (Marks and Houze 1987), the slope of the RMW does not coincide with the slope of azimuthal mean of reflectivity (Figs. 5 and 6). All five simulations showed that this result also held for updraft speed and vertical vorticity, which all appeared to be more upright (i.e., smaller slope) than the RMW (Figs. 5 and 6). For updrafts, slopes ranged between 50° and 65° for the three finer-resolution runs compared to about 75° for the two coarser-resolution cases while simulated RMW slopes ranged from ~75° for the 3–1-km case to ~80° in the 15–5-km case. Yang et al. (2007) showed that storms with larger eyewall tilt (or slope) were more intense because this tilt allowed more low-θ_e downdraft air to reach the subcloud inflow layer which in turn increased the air–sea entropy difference there and therefore, the energy input from the sea. They suggested that storms exhibiting less vertical tilt (smaller eyewall slope), were less intense because of enhanced inward potential vorticity (PV) mixing from the eye to the eyewall. Our results show, however, that despite larger eyewall slopes, the coarser-resolution cases still do exhibit relatively similar intensity to those at finer resolution.

The radius–height mean diagrams in Figs. 5 and 6 show that the horizontal gradients of Vt_θ, vertical vorticity (ζ_θ), and vertical wind (W_θ), increase as Δx, Δy decreases at all levels. Moreover, closer investigation of the reflectivity field shown in Fig. 4 revealed the existence of small-scale convective features of about 1–2-km depth near the surface (only observed for the 3–1- and 6–2-km case) on the inner boundary of the eyewall that were sometimes associated with well-defined isolated
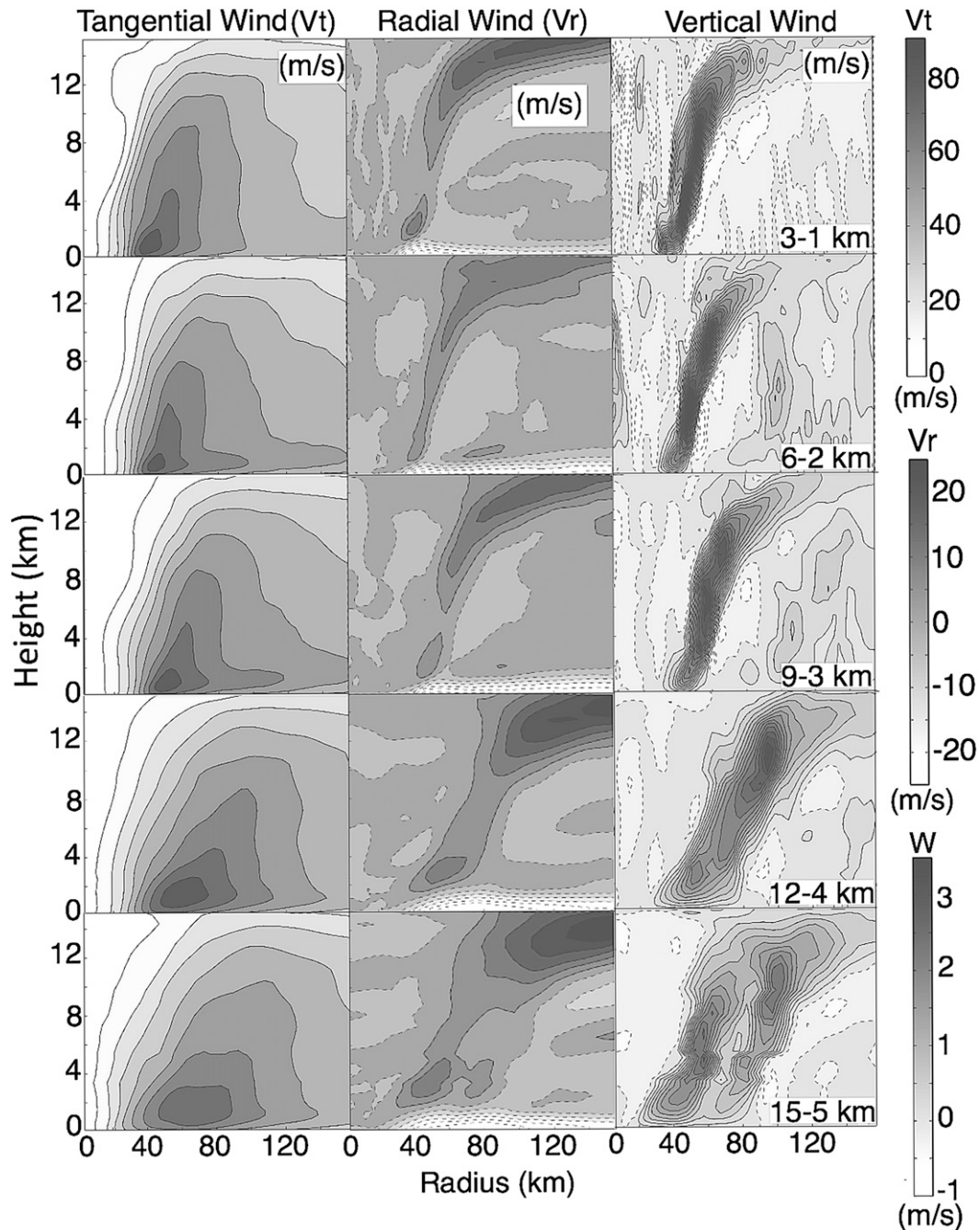
FIG. 5. Height–radius plots of mean azimuthal tangential, radial, and vertical wind speed (m s^{-1}) for the five cases at 1200 UTC 23 Sep 2005. The dotted lines in the third column for vertical wind speed depict the 0 m s^{-1} contour. The legends for shadings are shown on the right-hand side of the figure.

maxima in wind speed, sometimes reaching 100 m s^{-1} in the simulation (not shown), consistent with previous modeling work (Yau et al. 2004) and in situ observations (Aberson et al. 2006; Marks et al. 2008).

The updrafts in all five cases exhibit a *bimodal* distribution with two well-defined maxima: one below the

freezing level (4–5 km) and another one near or above 8 km (Fig. 5). This result is consistent with previous observational and modeling studies made in mature hurricanes (Black et al. 1996) and tropical maritime squall lines (Samsury and Zipser 1995; May and Rajopadhyaya 1996; Fierro et al. 2008, 2009). The 6-km simulation of
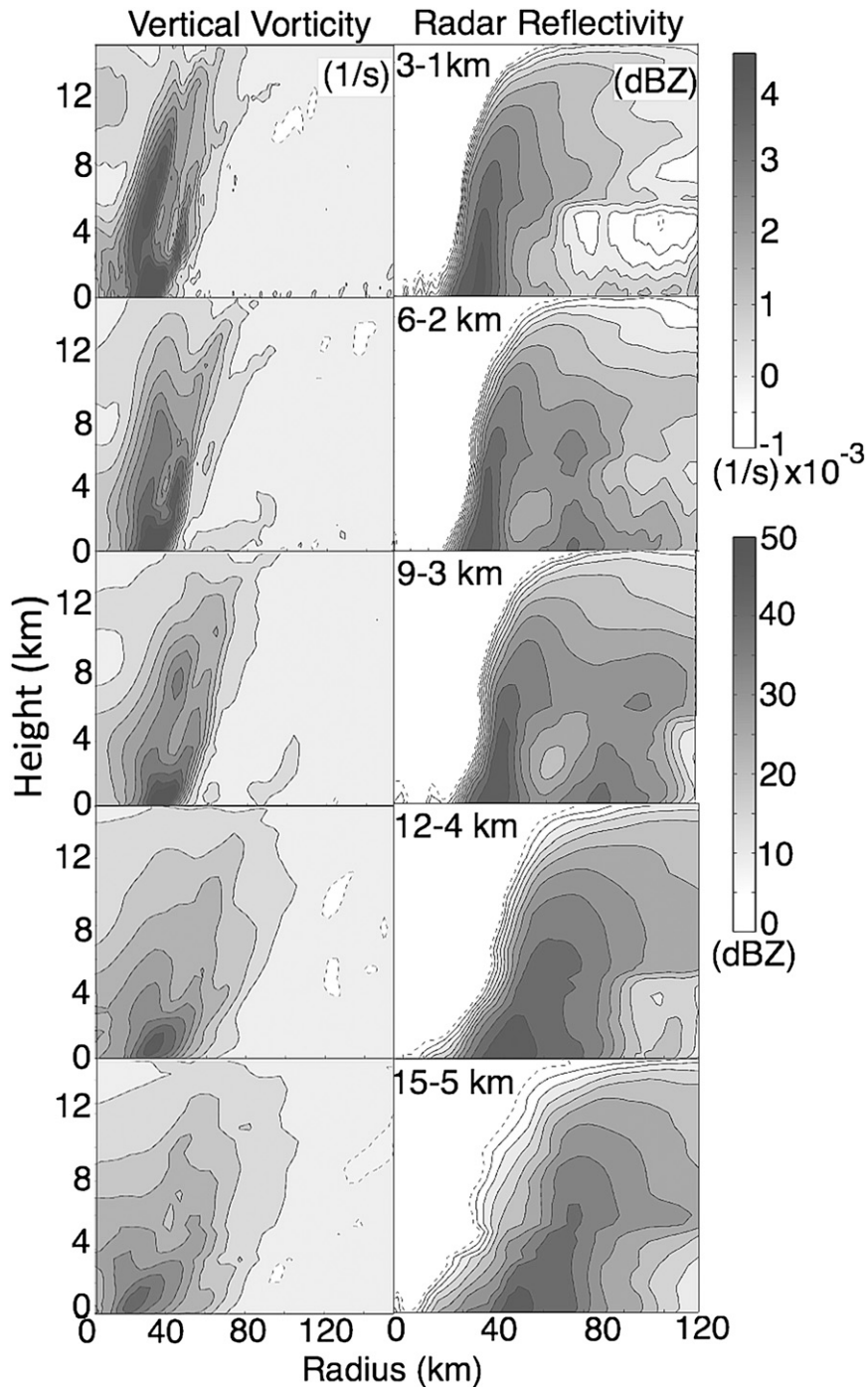
FIG. 6. As in Fig. 5, but for vertical vorticity ($\times 10^{-3}$ s^{-1}) and radar reflectivity (dBZ). Note that for vertical vorticity the radial axis extends to near 160 km compared with 120 km for radar reflectivity.

Liu et al. (1999) also showed evidence of this bimodal distribution (their Fig. 15c) but the latter was never discussed. Previous studies suggested that the lower maximum is mainly attributed to dynamical forcing

(frictional convergence for hurricanes and gust front upward directed hydrostatic pressure gradient force for squall lines), while the upper-level maximum could be a consequence of water unloading and buoyancy
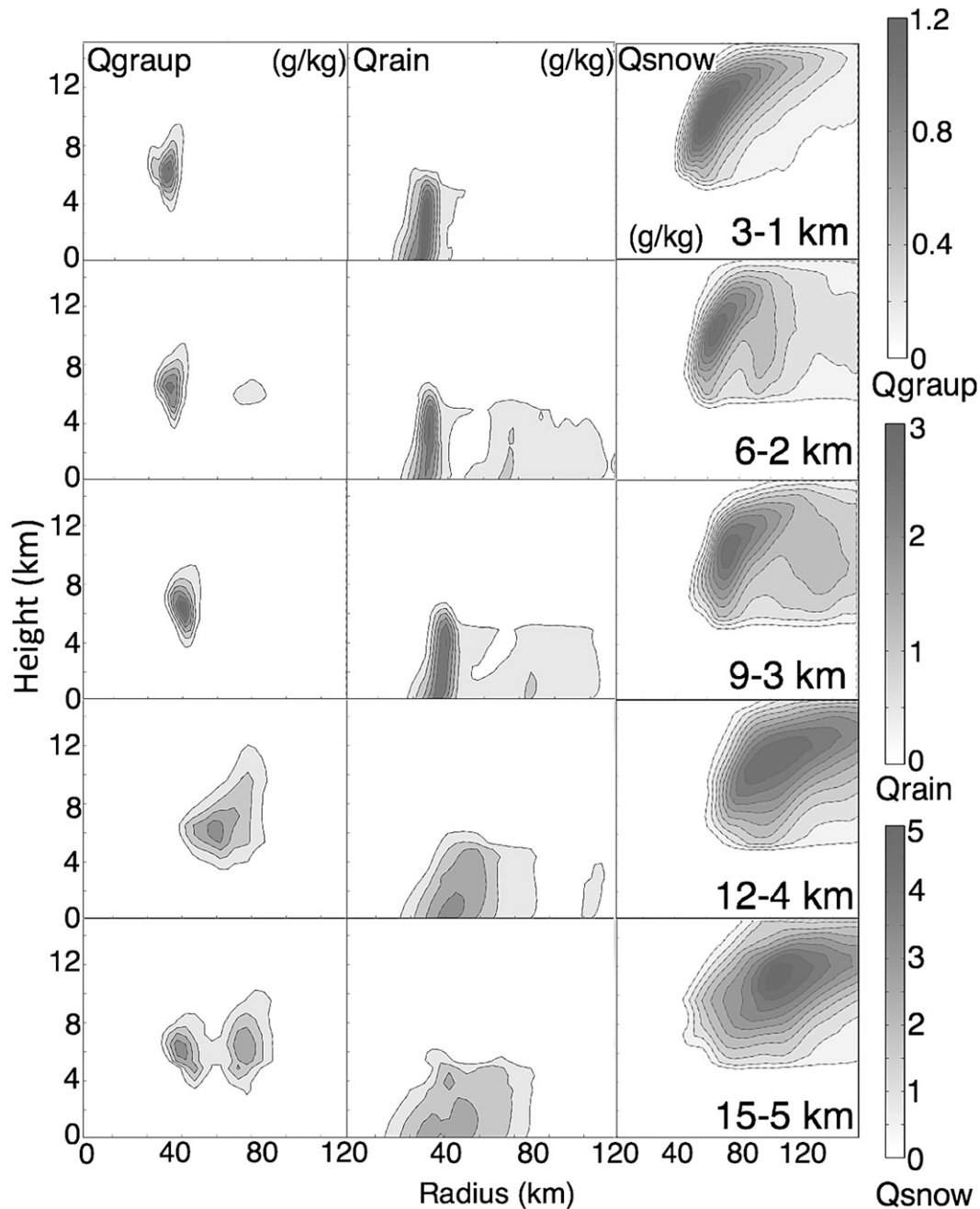
FIG. 7. As in Fig. 5, but for graupel, rain, and snow mixing ratio (g kg^{-1}). Note that the radial axis for snow mixing ratio extends to 160 km instead of 120 km for graupel and rain mixing ratio.

(Samsury and Zipser 1995; May and Rajopadhyaya 1996; Trier et al. 1996; Zipser 2003; Fierro et al. 2008, 2009). Black et al. (1996) found in hurricane eyewalls a relative minimum in updraft speed near 6 km, which agrees remarkably well with the results obtained herein for W_θ, particularly in the two finer-resolution cases (Fig. 5). The double maximum in vertical velocity with radius that is present in the 15–5-km simulation exists because the storm-centered circles along which the azimuthal mean is computed covers a wavenumber 4 eyewall asymmetry (Fig. 4). This double maximum in vertical wind is however not present in the 12–4-km case because the amplitude of the wavenumber 2 eyewall asymmetry in this simulation is too large (i.e., large eccentricity) for those circles to cover it entirely (Fig. 4).
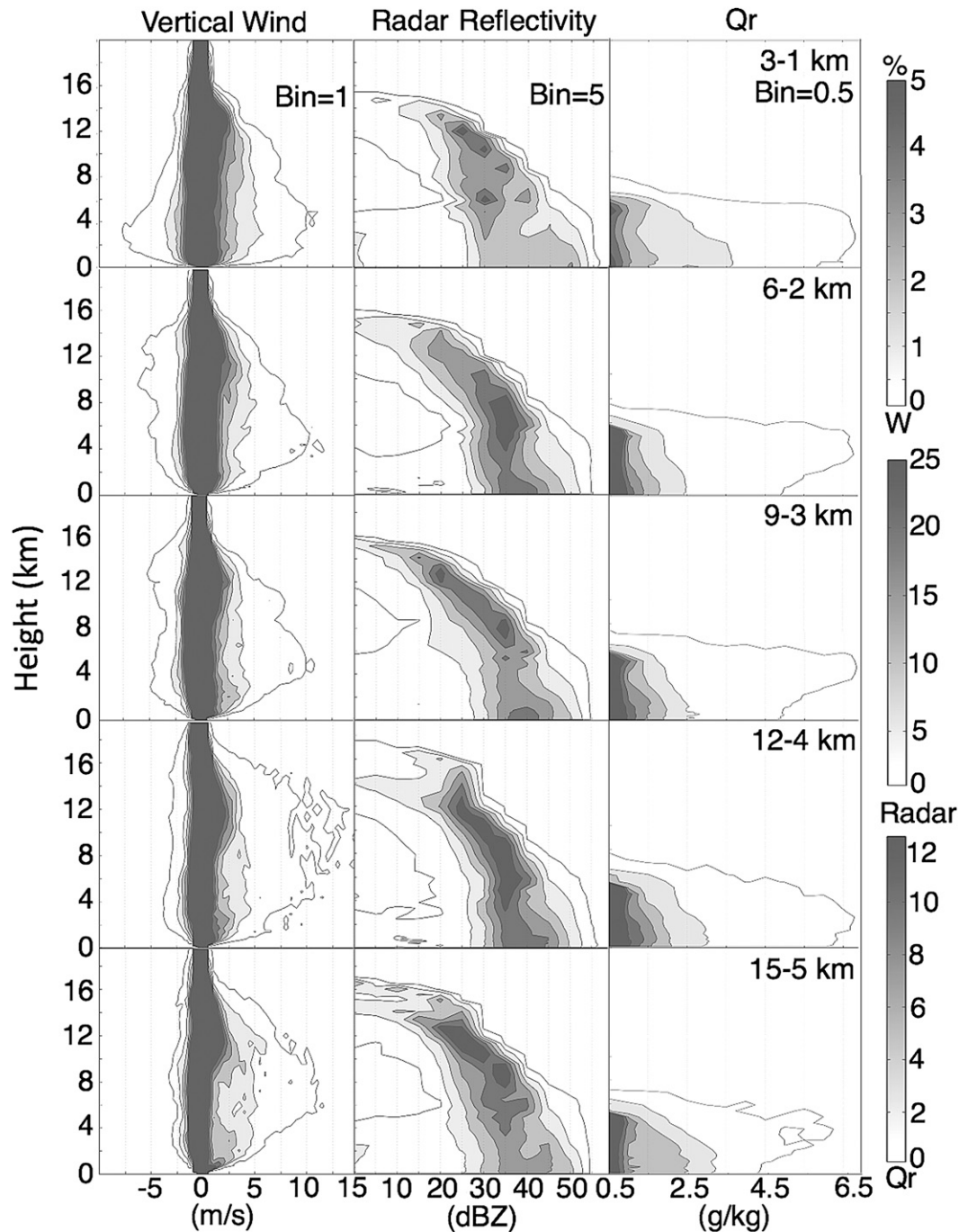
FIG. 8. CFADs of vertical wind (W; m s^{-1}), radar reflectivity (dBZ), and rain mixing ratio (Qr; g kg^{-1}) in bins of 1 m s^{-1}, 0.5 g kg^{-1}, and 0.5 g kg^{-1}, respectively, for all five cases at 1200 UTC 23 Sep 2005. Legends for shadings are shown on the right side of the figure.

The *depth* of the inflow layer (defined as the layer containing negative azimuthally averaged radial wind) decreased as resolution increased (Fig. 5). In fact, under the eyewall, this depth doubled from about 1 km in the 3–1-km case to about 2 km in the 15–5-km case. Furthermore, the coarser-resolution cases produced

larger azimuthally averaged radial wind speed (by about 5 m s^{-1}) in this inflow layer near the surface (Fig. 5). Computations of the vertical mass flux and inflow mass flux in Table 2 for all five cases showed that at coarser resolution, the simulated storms produced much larger low-level inward mass flux, which by virtue
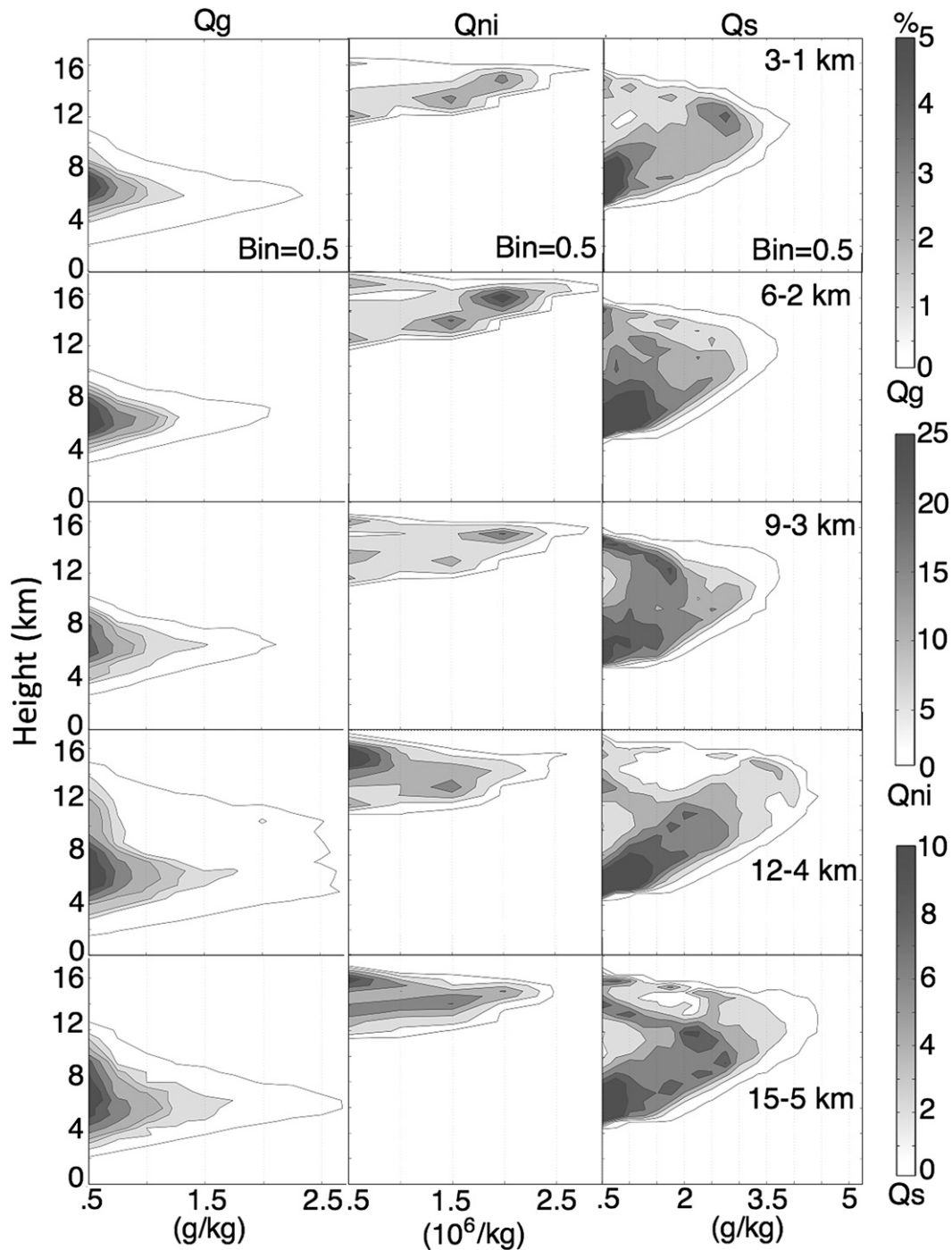
FIG. 9. As in Fig. 8, but for graupel mixing ratio (Qg), snow mixing ratio (Qs; g kg^{-1}), and number ice concentration (Qni; 10^6 kg^{-1}) in bins of 0.5 g kg^{-1}, 0.5 g kg^{-1}, and 0.5×10^6 kg^{-1}, respectively.

of mass conservation must be consistent with larger vertical (i.e., updraft) mass flux in the eyewall. This shows that at coarser resolution, the secondary circulation is stronger, which is consistent with larger sensible heat/moisture flux and favorable for storm intensity. Therefore, it appears that at coarser resolution, the larger areal coverage of strong radial surface fluxes (consistent with a deeper and stronger secondary circulation) is able to counteract the detrimental effects of smaller radial gradients and internally generated eyewall asymmetries, resulting in storms of relatively similar intensities.

Overall, the simulated microphysical structures are qualitatively consistent with past modeling studies at similar horizontal resolution (Liu et al. 1997; Wang 2002a; Fierro et al. 2007). As expected from the profiles of axisymmetirc kinematic variables, the three finer-resolution cases again exhibited larger values of axisymmetric rain, graupel, and snow mixing ratio (e.g., Qr_θ, Qg_θ, and Qs_θ; Fig. 7) and hence axisymmetric radar reflectivity (dBZ_θ; Fig. 6). Most importantly, the latter variables exhibited sharper radial gradients at the inner edge of the eyewall as horizontal resolution increased. The reflectivity in the 3–1-km case quickly decreases radially outward to values below 10 dBZ. On the other hand, the 6–2- and 9–3-km cases showed evidence of well-defined secondary azimuthally averaged reflectivity maximum at radii of 60 and 80 km, respectively. This secondary reflectivity maximum (also see in Fig. 4) is coincident in space with weak maxima in W_θ, Vt_θ, and ζ_θ (Figs. 5 and 6). Those characteristics are similar to the ones associated with secondary concentric eyewalls (Terwey and Montgomery 2008) and a moat region (referred to as filamentation zone by Rozoff et al. 2006) followed by a secondary wind maximum (e.g., Houze et al. 2007), which were shown to be associated with a temporary weakening of the storm (Willoughby et al. 1982) and that was actually observed for Hurricane Rita about a day earlier than shown in our simulations (Knabb et al. 2005).

In addition to looking at mean values or cross sections at a single level or location, it is also worthwhile to examine the properties of the entire distribution of a variable. This will allow a diagnosis of the impact of resolution on different portions of a distribution (e.g., to compare the impact of resolution on the percentage of updrafts that are strong versus weak). Figures 8–9 show contoured-frequency by altitude diagrams (CFADs: Fig. 5 in LeMone and Zipser 1980) for select variables. For the computation of the frequencies, the data was extracted within a box surrounding the eyewall relative to a storm center that was defined by the location of the minimum surface pressure. Since the two coarser runs had larger eyewalls, the box was allowed to cover a slightly larger area for those two cases. The distribution of vertical velocities varied significantly between the cases at this time. For example, as Δx and Δy increased, the frequency contour for the strongest (top 0.1%) updrafts tends to shift toward higher altitudes (Fig. 8), while the 0.1% contour of downdrafts reached larger values in the three finer-resolution cases between 0 and 4 km (particularly for the 3–1-km case with values near -5 m s^{-1}). Generally speaking, the updraft distribution in the eyewall for all five cases agree well with the composite observations of Black et al. (1996), who found

that the vast majority of vertical motions were weak ($|w| < 2$ m s^{-1}), although the model seems to produce generally fewer strong updrafts than what have been found in Black et al. (1996). Those results are similar to those of R07 but seem to contradict those of McFarquhar et al. (2006) who found in their 2-km MM5 simulation more strong updrafts than observed above 9 km. In nature, about 1%–2% of the drafts exceed 5 m s^{-1} (Black et al. 1996), which is in good agreement with our results (lightest gray shaded contour in Fig. 8) and those of R07. In all five cases, the distribution of updraft speeds does not broaden with height as in the observations, indicating that the strongest updraft cores weaken with height. This result is similar to previous modeling results such as R07. The two coarser-resolution cases have their small frequency contours (top 0.5%) extending toward larger updraft values (>10 m s^{-1}), which is consistent with stronger secondary circulations (Table 2). At even coarser resolution (Δx and $\Delta y \geq 10$ km) the top 0.5% contour dropped below 5 m s^{-1}, which is consistent with overall weaker axisymmetric vertical velocities (not shown).

In contrast with observations in mature hurricanes, none of the five cases presented herein exhibited a sharp decrease of reflectivity above the melting level (Fig. 8), similar to the results of R07. In all cases, we noted an increase of larger frequencies greater than 2% of 20–25- and 25–30-dBZ reflectivity bins above 8 km, associated with an overall small amount of graupel and water drops and the predominance of snow particles at those levels (Fig. 9). In nature, both Atlantic hurricanes and tropical convective clouds exhibit a sharp decrease of radar reflectivity (and therefore frequencies of larger reflectivity bins) above the melting level (R07), with maximum values in the vast majority of the cases seldom exceeding 50 dBZ (e.g., Marks et al. 2008). The rapid decline of reflectivity values above the freezing level is mainly attributed to warm rain processes, which leaves very little supercooled water available in the mixed-phase region (between 0°C and -20°C) for the formation/growth of graupel and hail (e.g., Black and Hallett 1986). In line with R07, McFarquhar et al. (2006) and Davis et al. (2008) we observed a high bias of radar reflectivity particularly for values larger than 40 dBZ near the surface.

In contrast to the three finer-resolution cases, the 15–5- and 12–4-km cases produced a deeper distribution of graupel with altitude. This indicates that the stronger secondary circulation in the coarser runs carried graupel over a deeper layer, supporting larger volumes of mixed-phase particles (and therefore latent heating) aloft that are indicative of strong updrafts (Wiens et al. 2005) generally exceeding 10 m s^{-1} (McFarquhar et al. 2006). The 6-km simulation of Liu et al. (1999) also consistently
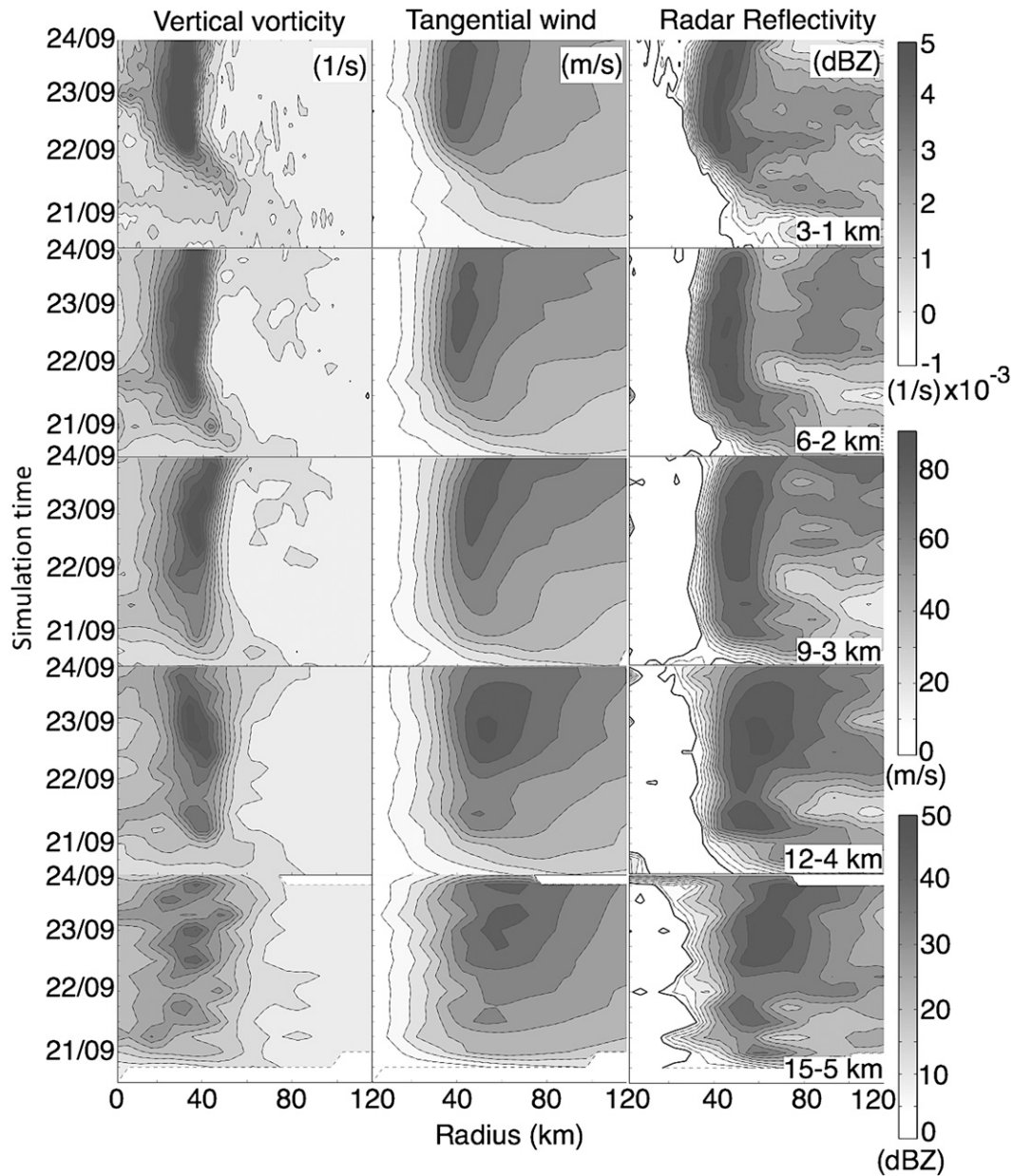
FIG. 10. Hovmöller diagrams of azimuthally averaged vertical vorticity ($\times 10^{-3}$ s^{-1}), tangential wind (Vt; m s^{-1}), and radar reflectivity (dBZ) at $z = 1.12$ km. Legends for shadings are shown on the right side of the figure.

produced graupel (0.5 g kg^{-1}) at rather high altitudes near 250 hPa. Although the frequency distribution of snow (and rain) did not exhibit marked trends or differences, there is some indication that the wider eyewalls in the two coarser-resolution cases did produce more snow: the 0.1% contour for snow reached higher mixing ratio values (near 8.5 g kg^{-1}) for the coarse runs than for the fine runs (7.5 g kg^{-1}; Fig. 9). All cases showed a well-defined maximum in the frequency of snow mixing ratio between 0.5 and 1.5 g kg^{-1} between

4 and 8 km (Fig. 9), which is consistent with largest frequencies of 0.5–1 g kg^{-1} graupel mixing ratio as more snow particles are available for graupel growth by rime accretion (Fig. 9). Note that in all five cases a very small volume (only about 2% of the sampled grids) had a graupel mixing ratio of about 1 g kg^{-1}, consistent with in situ observations (McFarquhar and Black, 2004). Near the homogeneous nucleation level (at about −40°C near $z = 15$ km) the three finer-resolution runs produced higher frequencies of large values of number ice
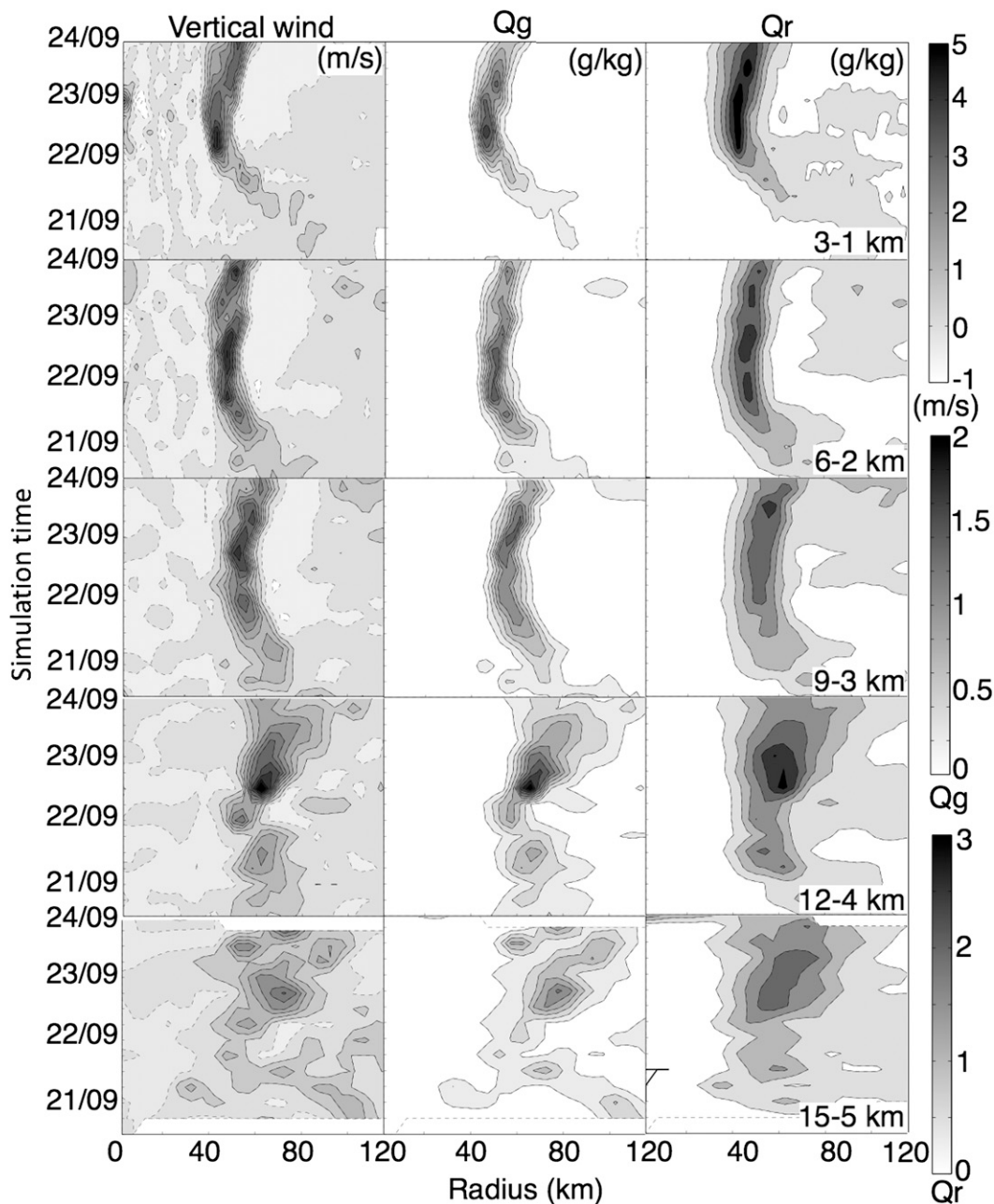
FIG. 11. As in Fig. 10, but for azimuthally averaged vertical wind speed (W; m s^{-1}), graupel mixing ratio (Qg; g kg^{-1}) at $z = 5.91$ km, and rain mixing ratio (Qr; g kg^{-1}) at $z = 1.12$ km. The dotted line in the W plots marks the zero contour.

concentration (Qni; 2×10^6 kg^{-1}; Fig. 9), while the two coarser cases had larger frequencies toward smaller Qni values (0.5×10^6 kg^{-1}). Aircraft penetrations in Hurricane Humberto (2001) at temperatures near $-40°$C revealed maximum ice particle size concentrations ranging between 200 and 300 L^{-1} (Heymsfield et al. 2006), which is equivalent to about 1.2 and 1.8×10^6 kg^{-1} when accounting for density variations with altitude. Hence, the

modeled values at finer resolution tend to agree better with observations.

c. Kinematic and microphysical evolution during the intensification phase

After focusing on the spatial structure of the simulated storm at a single time, this section will be devoted to its temporal evolution, which will help to further

identify factors promoting/limiting storm intensity. To provide a comprehensive view of the kinematic and microphysical evolution, we generated time–radius (i.e., Hovmöller) plots of axisymmetric means, where the storm's center is defined at each altitude as the minimum in the smoothed geopotential field. Allowing the storm center to vary with height will mask some of the asymmetries in the vertical and in the horizontal that many observational and modeling studies have suggested are essential to hurricane intensity and motion (e.g., Marks et al. 1992; Liu et al. 1999; Shapiro and Franklin 1999; Reasor et al. 2000; Rogers et al. 2003; Nolan et al. 2007).

The 3–1-km simulation develops a well-defined ($>5 \times 10^{-3}$ s^{-1}) ring of positive azimuthal-mean vertical vorticity (ζ_θ) at $z = 1.12$ km 36 h into the simulation (hereafter the subscript θ refers to azimuthally averaged variables; Fig. 10). While the magnitude of this vorticity is larger than the other four runs, its development occurs later than the other runs. The RMW varies from ∼40 to ∼60 km in the 3–1- and 15–5-km cases, respectively, with even larger values for Δx, $\Delta y \geq 10$ km (e.g., ∼90 km for the 60–20-km run, not shown). Aircraft data found that the eye diameter was about 35 km at Rita's peak intensity (Knabb et al. 2005), so the observed RMW was about 10 km smaller than the smallest RMW in the 3–1 km run. Previous modeling studies have often produced generally larger simulated RMW's compared to the observations while still producing pressure minima and wind speed maxima similar to observations (e.g., R07; Fierro et al. 2007). Davis et al. (2008) suggested that storm size was likely influenced by model resolution (and drag formulation) and increased as Δx, Δy increased, as suggested by Liu et al. (1999) and shown by Yau et al. (2004). Kimball and Mulekar (2004) found that the median RMW decreases with storm intensity, from about 60 km for category 1 storms to 40 km for category 5 storms. However, a recent analysis of in situ observations of hurricane wind fields by Stern and Nolan (2009) has shown that there is a strong relationship between the size of the RMW and the slope of the eyewall, where larger (smaller) RMWs are associated with larger (smaller) slopes; they also found that neither storm size nor eyewall slope is correlated with intensity. Stern and Nolan (2009) also found that the RMW–slope relationship, as well as its independence from intensity, could be shown explicitly from the maximum potential intensity theory of Emanuel (1986). A similar relationship was seen for these runs (Figs. 5 and 10). This suggests that the WRF-ARW model captures this essential aspect of storm dynamics as resolution varied between 1 and 5 km.

All cases behave qualitatively the same; the increase in Vt$_\theta$ and ζ_θ (at 1.12 km) during intensification is coincident with an increase in the azimuthal mean

of graupel mixing ratio (Qg$_\theta$), rain mixing ratio (Qr$_\theta$), radar reflectivity (dBZ$_\theta$), and vertical velocity (W$_\theta$; Figs. 10 and 11) suggesting that storm becomes better organized and circular. For all these variables, the three finer-resolution runs exhibited overall better-defined radial profiles (cf. Figs. 5–8) in the eyewall throughout the simulation, consistent with radial gradients being better resolved, which would promote storm intensity.

To see how the mean properties of certain fields evolve in height and time, we computed time–height plots of updraft and downdraft mass fluxes above or below a predefined threshold within a predefined box, which dimensions were selected such that the box covers the eyewall (and eye). Also, because eyewall convection sloped outward, we used vertical cross sections to determine the dimensions of this predefined box to ensure that the latter also contained the upper-level updrafts and a good portion of the outer eyewall stratiform region. For microphysical quantities, we used a different approach and computed time–height volume plots in the following manner: for each grid point having any given variable equaling or exceeding a preset threshold value we counted the volume occupied by that grid element using an average value of dz (i.e., 472 m) based on the model top and number of grid points in the vertical (as in Fierro et al. 2006). The advantage of using hydrometeor volumes over hydrometeor mass fluxes is that the latter involves the product of mixing ratio and vertical velocity, while volumes just make use of mixing ratio. In our context, this makes comparisons among cases easier as hydrometeor volumes are more directly related to hydrometeor content or mass. Information about the vertical distribution of total microphysical quantities will provide key insight on the temporal evolution of the vertical distribution of latent heat (e.g., Gray 1995) and therefore PV (e.g., Yang et al. 2007).

As expected from overall larger eyewalls and wider updrafts, the two coarser runs exhibit much larger total updraft mass flux, updraft mass flux for updrafts ≥ 5 m s^{-1} (W5), and total downdraft mass flux than the three remaining cases at almost all levels (particularly above 7 km; Fig. 12a). Consequently, the 0.5 g kg^{-1} rain mixing ratio (Qrvol), 0.5 g kg^{-1} graupel mixing ratio (Qgvol), and 30-dBZ echo (dBZvol) volume were larger in the two coarser-resolution runs (Fig. 13) and are consistent with the CFADs for graupel and rain showing increased frequencies toward larger values (Figs. 7 and 8). These further support the notion that at coarser resolution the simulated storms exhibit stronger secondary circulations, which carry a larger volume of condensate aloft and therefore produce more latent heating. The simulated eyewall total downdrafts and updraft mass flux values are comparable to those observed by Black et al.
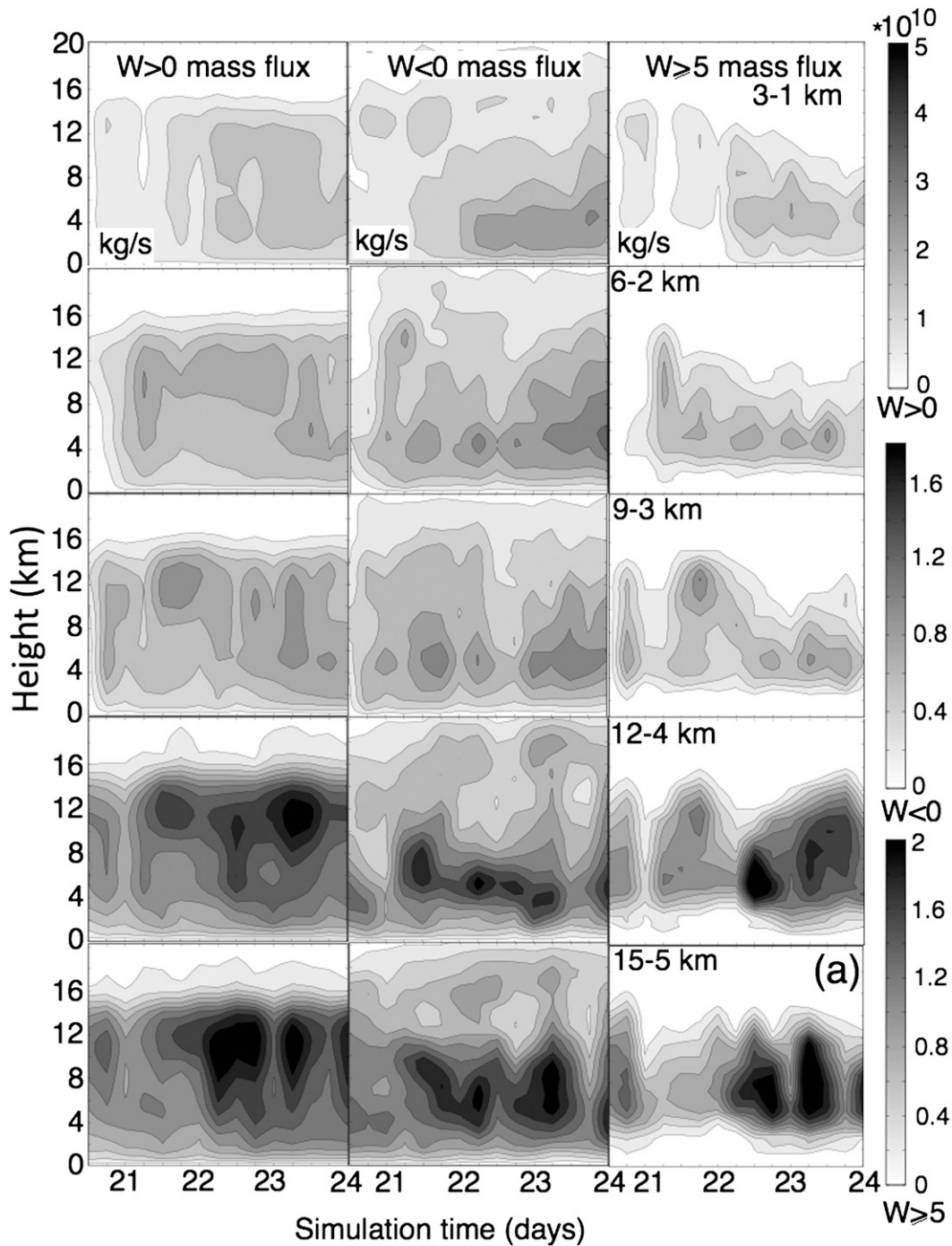
FIG. 12. (a) Time–height plots from left to right of total updraft mass flux, total downdraft mass flux, and updraft mass flux for updrafts ≥ 5 m s^{-1} (kg s^{-1}) for the five cases within a predefined box containing the eye and eyewall. Legends for shadings are shown on the right side of the figure. (b) From left to right the fraction of the mass flux for updraft ≥ 1 m s^{-1} (W1) relative to the total updraft mass flux (W+), the mass flux for updraft ≥ 5 m s^{-1} (W5) relative to W+ and the mass flux for downdrafts ≤ -2 m s^{-1} (W$-$2) relative to the total downdraft mass flux (W$-$).
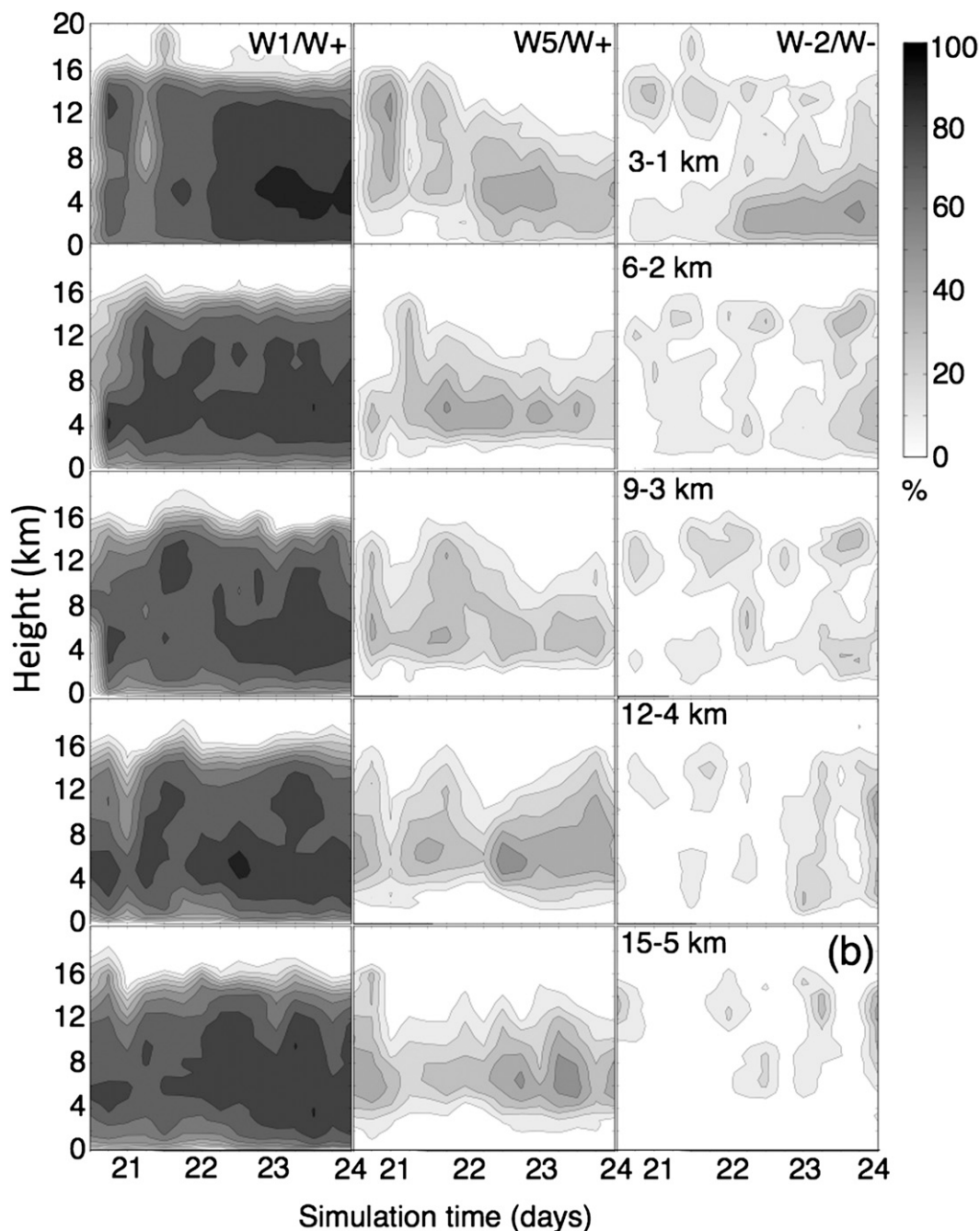
FIG. 12. (*Continued*)

(1996, their Fig. 16), after accounting for the fact that the Black et al. (1996) vertical mass fluxes were scaled by a factor of 2π (their formulas 3 and 4) due to the use of cylindrical coordinates. As Δx, $\Delta y \geq 10$ km, the total updraft fluxes and hydrometeor volumes progressively became smaller, consistent with a weaker secondary circulation (Table 2) and overall weaker vertical velocities (not shown).

The simulations revealed that updrafts ≥ 5 m s^{-1} did show a remarkably similar contribution to the total updraft mass flux in all five cases: below 3 km, their contribution was less than 10% while between 4 and 8 km, they contributed to between 30% and 50% of the total updraft mass flux (Fig. 12b), which is in good agreement with Jorgensen et al.'s (1985) statistics of in situ observations within mature hurricanes (their Fig. 7). Perhaps
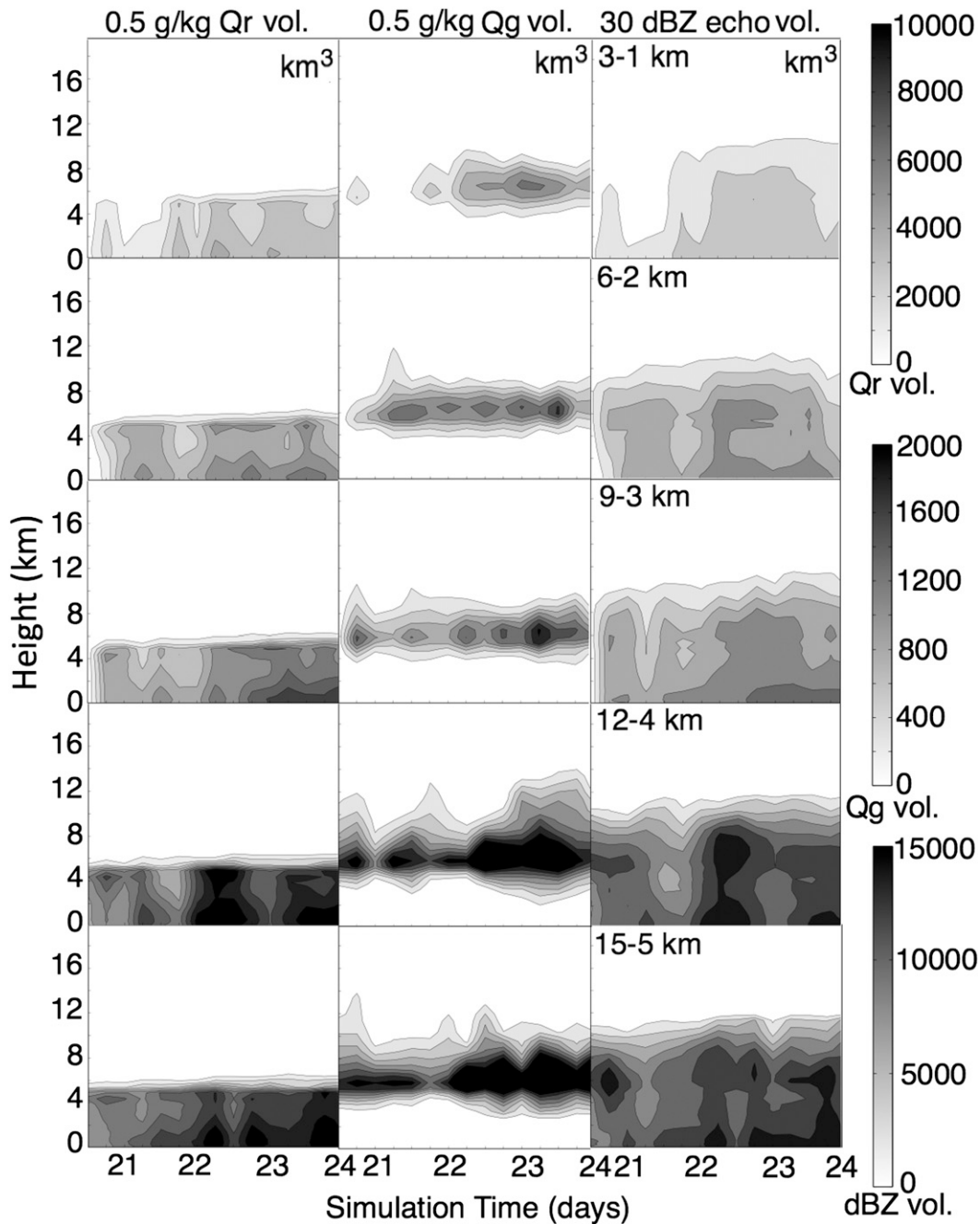
FIG. 13. Time–height plots of 0.5 g kg^{-1} rain mixing ratio volume, 0.1 g kg^{-1} graupel mixing ratio volume, and 30-dBZ echo volume in km^3 within a predefined box containing the eye and eyewall. Legends for shadings are on the right side of the figure.

the most striking result from this particular analysis is that the 3–1 km case had by far the largest contribution to its total downdraft mass flux below the melting level by downdrafts ≤ -2 m s^{-1} (Fig. 12b) and largest -2 m s^{-1} downdraft volume (not shown). Consistent with the presence of more downdrafts in the finest-resolution case, closer inspection revealed that, particularly inside the

eye, the 3–1-km case exhibited a deeper layer of drier air than all the other cases: For instance, the 10% relative humidity contour extends from 4 to 16 km in the 3–1-km storm compared to between only 8 and 12 km in the 15–5-km case (Fig. 14). Furthermore, as Δx, Δy was increased at (Fig. 14) and above 10 km (not shown) the relative humidity in the eye exceeded 40%, which is
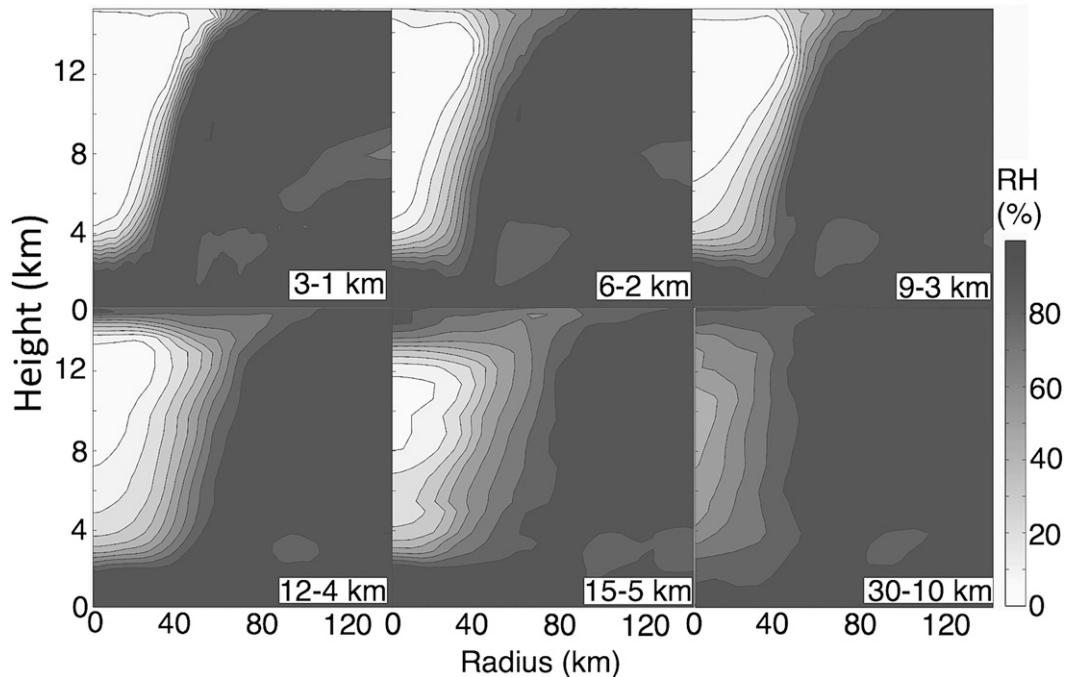
FIG. 14. As in Fig. 5, but for relative humidity (%).

consistent with weaker secondary circulations (Table 2) and weaker storms (Fig. 2). This drier air at finer resolution is also reflected in the equivalent potential temperature (θ_e) profile. The simulated minimum in the 3–1-km run (near 358 K) was about 10° lower than the 15–5-km case (about 369 K, not shown). A subsequent study using trajectory analysis with relatively finer temporal resolution than used herein (1 h or less is desired) will be performed in the near future to address if the downdrafts in the eye are the cause or the consequence of the presence of this deeper layer of drier air and in turn determine to what extent this dry air mixes with the eyewall convection and influences downdraft potential and storm intensity.

In the previous section, we showed that during the steady-state period, the coarser-resolution cases exhibited larger-amplitude eyewall asymmetries (cf. Fig. 4), which has been shown to act as a potential brake on storm potential intensity (Peng et al. 1999; Wu and Braun 2004; Yang et al. 2007). Therefore it is relevant to determine their temporal evolution and persistence. To quantify the amplitude of the eyewall asymmetries and their evolution, we carried out a fast Fourier transform (FFT) on the radar reflectivity at $z = 1.5$ km averaged along circles at and inside about 10 km of the RMW (Fig. 15), similar to what was done in radar observations of Hurricane Elena (1995; Corbosiero et al. 2006). Recently, Murillo et al. (2009, manuscript submitted to *Mon. Wea. Rev.*) compared single Doppler retrieved

wavenumber 0 and 1 reflectivity and wind structures for Hurricane Danny (1997). They pointed out that while the wavenumber 0 structures were similar the phase and amplitude on the wavenumber 1 asymmetries were not. In the light of those results, an additional FFT analysis was carried out on the simulated horizontal wind speeds ($z = 1$ km) and revealed that the results were almost identical to those using radar reflectivity (not shown). We will focus our analysis after 0000 UTC 22 September 2005, which is the time when the simulated storms exhibited a well-defined eyewall in all five cases. We noticed that, particularly in the three finer-resolution cases, the darkest shaded contours (indicating high power ratio relative to the azimuthal mean) are essentially confined in the axisymmetric flow and wavenumber 1 asymmetry, which shows that most of the variance (or power) in the reflectivity field is contained in the axisymmetric mean and wavenumber 1 asymmetries. Those results are similar with what previous studies have found for the horizontal flow within observed hurricanes (Lee et al. 1994, 2000; Roux and Marks 1996; Reasor et al. 2000; Lonfat et al. 2004; Corbosiero et al. 2006). Most importantly, relative to the highest power, the two coarser cases have a higher proportion of large power values contained in wavenumber 1, 2, and 3 asymmetries, indicative of larger amplitudes of these asymmetries, a result that is consistent with Gentry and Lackmann (2010). Those larger-amplitude eyewall asymmetries explain why axisymmetric means are generally smaller in the two coarser cases
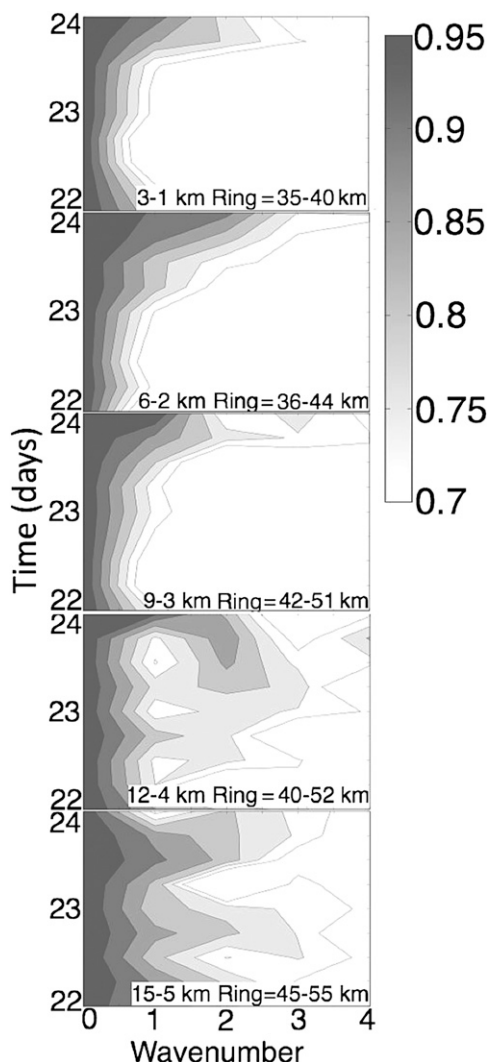
FIG. 15. Fourier spectral decomposition of eyewall wavenumber asymmetries of radar reflectivity at $z = 1.5$ km averaged along several circles centered at the minimum geopotential height. The ring where the average was carried out is shown at the bottom. The dark filled contour show the log-10 of Fourier coefficient power divided by the log-10 power of the azimuthal mean. Legends are shown on the right side of the figure.

(Figs. 10 and 11). Additional power spectra plots that extend to higher wavenumbers (i.e., greater than 6) revealed that the 3–1-km case exhibited larger power values for these high-wavenumber asymmetries than the coarse runs, though the magnitude of the power is much less than the lower-wavenumber asymmetries (not shown). At even coarser resolution, $(\Delta x, \Delta y \geq 10$ km), the majority of the eyewall asymmetries power was contained in wavenumber 1 (not shown). This tendency toward lower wavenumber at coarser resolution is mainly due to the poor azimuthal resolution in the eye, which can adequately resolve only the lowest wavenumbers. Schubert

et al. (1999) also showed that lower wavenumbers are favored for wider eyewalls. Modeling (Kossin and Schubert 2001; Wang 2002b) and observational (Kossin and Schubert 2004; Montgomery et al. 2006) studies have suggested that those eyewall asymmetries were associated with vortex Rossby waves or coherent vortices along the inner edge of the eyewall convection.

4. Discussion and conclusions

In summary, we found that changing the horizontal grid spacing from 5 to 1 km did not result in significant changes in maximum intensity (defined as the 10-m maximum wind speed and minimum sea level pressure), while in contrast, noteworthy differences in the simulated storms' kinematics and microphysics were found. Those structural differences were consistent through both the intensification and steady-state periods. Larger grid spacing resulted in larger eyewalls producing larger mass flux and volume of updrafts and, consequently, larger volumes of condensate, and ice-phased particles. In contrast, the opposite was true for downdrafts ≤ -2 m s^{-1}, which were found to produce by far the largest contribution to the total downdraft mass flux at finer grid spacing. Although the coarser-resolution cases consistently produced larger mass flux of updrafts ≥ 5 m s^{-1}, it was found that their contribution to the total mass flux varied little among the five cases. Hence, in all cases the bulk of the mass is being transported by the smaller drafts (and secondary circulation). The RMW and eyewall slope (defined as the axis of maximum Vt_θ) were also shown to increase as horizontal grid spacing increased, which is consistent with observations showing that eyewall slopes increase as RMW increases (Stern and Nolan 2009).

Vertical profiles of microphysical and kinematical variables at finer grid spacings were generally radially thinner as smaller updrafts were better resolved. The smaller azimuthal means of these variables at coarse resolution were attributed to larger-amplitude lower-wavenumber eyewall asymmetries, while at finer grid spacing, the eyewall asymmetries were of lower amplitude and higher wavenumber (greater than 6).

The simulations also revealed structural similarities among the five cases, which held during both the intensification and steady-state periods. For instance, all storms exhibited a bimodal updraft distribution and were able to reproduce the basic aspects of the primary and secondary circulation. Also, all cases produced relatively similar vertical distribution of rain, snow, and radar reflectivity in their eyewall.

One way to test the robustness of the differences shown here is to compare the structures produced from models of different resolution on a uniform grid. This
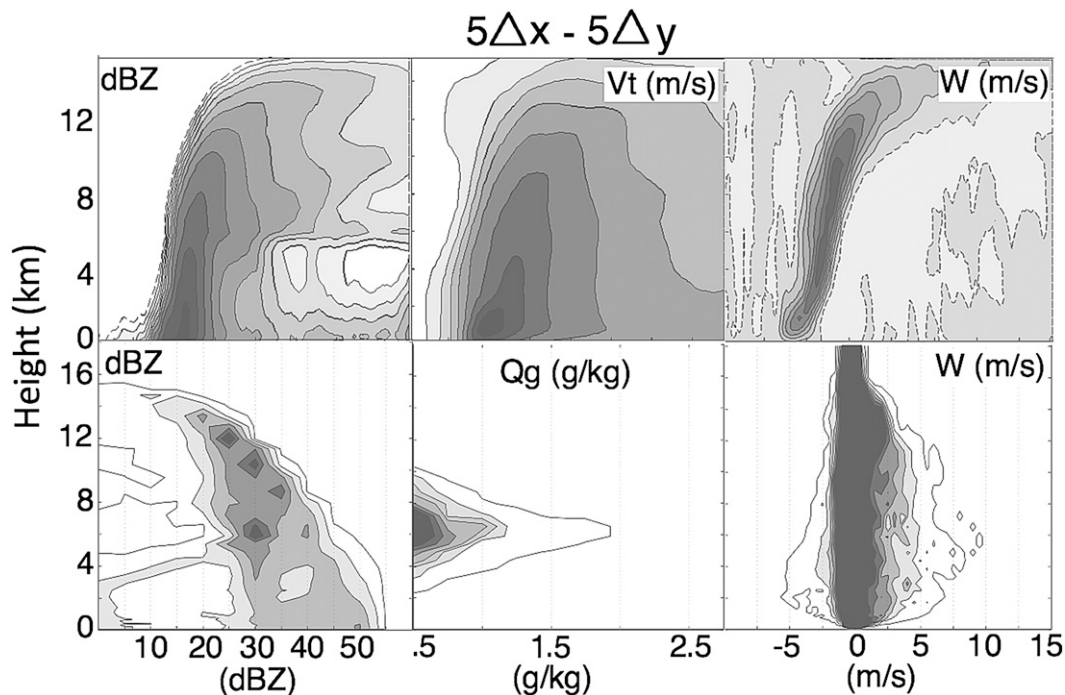
FIG. 16. Radius–height mean diagrams and CFADs for key variables of the 3–1-km case averaged onto a 5-km grid. Legends for contouring and shadings are the same as the above corresponding figures and are therefore omitted.

can be done by carrying out a volume average of the simulated fields of the finer grid onto the coarser grid (e.g., R07; Dr. J. Reisner 2009, personal communication). Figure 16 shows selected key fields averaged from the finest-resolution case (1-km inner mesh) onto a 5-km mesh (since Δz was identical, we carried out an areal average in this case), which facilitates a more direct comparison of the two simulations. When the volume-averaged profiles (CFAD and radius–height means) of the 1-km grid are compared with those of the 15–5-km case, we found that, similar to R07 (their Fig. 13), the averaging did not change the simulated profile significantly but rather smoothed out the fields and reduced the peak values/contours. Therefore, we can confidently affirm that the comparisons made herein remain valid.

An obvious question to ask based on these results is why the simulated storms showed little difference in intensity evolution between 1- and 5-km grid length despite noteworthy structural differences as a function of horizontal resolution. Across the (rather narrow) spectrum of resolutions compared in detail here, there were numerous factors that either limited or promoted storm intensification as resolution varied. For example, factors limiting storm intensification at coarser resolution were larger amplitude low-wavenumber eyewall asymmetries and smaller radial gradients, while the limiting factor at finer resolution was mainly a smaller areal coverage of larger

surface sensible and moisture fluxes. Conversely, factors favoring storm intensification at coarser resolution were the larger areal coverage of stronger surface fluxes (consistent with larger BL kinetic energy), while at finer resolution the larger radial gradients and smaller amplitude low-wavenumber eyewall asymmetries favored stronger storm intensity. Given the resultant similarity in intensity evolution, these factors must have compensated for each other, causing the simulated storms' intensities to be relatively similar for different resolution despite exhibiting noticeable structural differences.

In contrast, as Δx, Δy in the inner mesh was further increased from 10 km up to 30 km, the storm intensity showed a rapid decline: the strength of the secondary circulation, measured by the inflow mass flux and updraft mass flux, showed a progressive weakening (Table 2), which was consistent with smaller hydrometeor mass aloft (not shown) and weaker updraft speeds. A similar trend was simulated for the BL kinetic energy (Table 2), which also indicated progressively weaker near-surface wind fields. If we consider a typical eye diameter of 40 km, a mesh of 10 km would represent the lower limit at which the eyewall could be resolved. This limitation, together with much weaker radial gradients, are the likely causes for the storm intensity to drop off dramatically as Δx, Δy exceeds the 10-km threshold.

From the standpoint of accurately representing the kinematic and microphysical structures at different

horizontal resolutions, the finer-resolution cases, particularly 3–1 km, exhibited a more realistic storm, which suggests that horizontal resolution is important in resolving small-scale structures (Yau et al. 2004; Chen et al. 2007), some of which could be important in determining storm intensity (e.g., small-scale meso-vortices) and rapid intensity changes, which are currently poorly modeled (Davis et al. 2008). In the future, further studies at finer horizontal grid spacing (Δx, $\Delta y <$ 500 m) are needed to determine if our results hold because the flow characteristics were shown to change when Δx, $\Delta y < 250$ m (Bryan et al. 2003), with an increasing turbulent regime and increasing importance of entrainment effects. While these results were obtained in thunderstorm simulations, they should also be tested in hurricane environments.

At the range of cloud-resolving grid spacings used here it appears that axisymmetric differences in these structures *do not* translate to significant changes in the 10-m maximum wind speed. Again, similar analysis using finer grid spacings are required to determine if horizontal resolution alone (i.e., using similar physical parameterizations) can significantly improve intensity forecasts as posited by Houze et al. (2007). The current study suggests that this might not be the case and that, rather, more improvements in the representation of the model physics, particularly the atmospheric boundary layer (McFarquhar et al. 2006), and storm initialization using real-time data assimilation (as in Zhang et al. 2009) are needed to improve TC intensity forecasts. Further tests at higher horizontal resolution and with a variety of physical parameterizations and initial vortex structures for several strong storm cases are required to better address this hypothesis. Recently, using similar physics and settings within the ARW model, Gentry and Lackmann (2010) carried out a similar analysis for Hurricane Ivan (2004) and showed that as Δx, Δy, was increased from 1 to 6 km, the minSLP could differ by as much as 20 mb, while the structural differences as a function of horizontal resolution were comparable to those found here. Hence, while different physical/ dynamical processes influence modeled intensity and their respective weight vary as a function of Δx, Δy it seems that also the latter can change as a function of the storm case being studied.

Another reason why little difference was seen in the intensity of the simulated storms at different resolutions may be because of the way in which storm intensity is defined. If intensity were to be defined as the integrated surface (or even boundary layer) wind speed or kinetic energy, then the two coarser cases clearly produced "stronger" storms (Table 2). The wider and broader tropical storm force wind field observed in those two

cases would likely result in larger wind swaths and, therefore, more widespread and stronger storm surges. This result alone points out the misleading notion of using one metric to judge the performance of the model, particularly one not representative of the storm structure (e.g., 10-m maximum wind speed). Based on observations of mature hurricanes, the three finer-resolution cases tended to produce more realistic, "tighter" eyewalls with occasional rainbands, the latter being ill defined in the two coarser runs (as in Davis et al. 2008). Consequently the two coarser-resolution cases would tend to overestimate the simulated wind swath and storm surge, parameters that are critical when evacuation orders must be issued for coastal communities prone to storm surge. Moreover, structural details in the convection are also important when forecasting coastal and inland flooding. Our simulation showed that for instance the rainbands started to become better resolved at Δx, $\Delta y = 3$ km. Therefore, we suggest that in order to improve forecast of both, storm surge and flooding, a horizontal grid spacing of 3 km or less should be used in operational models.

REFERENCES

Aberson, S. D., M. T. Montgomery, M. Bell, and M. Black, 2006: Hurricane Isabel (2003): New insights into the physics of intense storms. Part II: Extreme localized wind. *Bull. Amer. Meteor. Soc.,* **87,** 1349–1354.

Black, M. L., R. W. Burpee, and F. D. Marks, 1996: Vertical motion characteristics of tropical cyclones determined with airborne Doppler radial velocities. *J. Atmos. Sci.,* **53,** 1887–1909.

Black, R. A., 1990: Radar reflectivity–ice water content relationships for use above the melting layer in hurricanes. *J. Appl. Meteor.,* **29,** 955–961.

——, and J. Hallett, 1986: Observations of the distribution of ice in hurricanes. *J. Atmos. Sci.,* **43,** 802–822.

——, and ——, 1999: Electrification of the hurricane. *J. Atmos. Sci.,* **56,** 2004–2028.

Braun, S. A., 2002: A cloud-resolving simulation of Hurricane Bob (1991): Storm structure and eyewall buoyancy. *Mon. Wea. Rev.,* **130,** 1573–1592.

——, and W.-K. Tao, 2000: Sensitivity of high-resolution simulations of Hurricane Bob (1991) to planetary boundary layer parameterizations. *Mon. Wea. Rev.,* **128,** 3941–3961.

Bryan, G. H., 2006: The dynamics of the trailing stratiform region of squall lines. Colloquium, National Severe Storms Laboratory.

——, and R. Rotunno, 2005: Statistical convergence in simulated moist absolutely unstable layers. Preprints, *11th Conf. on Mesoscale Processes,* Albuquerque, NM, Amer. Meteor. Soc., 1M.6. [Available online at http://ams.confex.com/ams/32Rad11Meso/techprogram/paper_96719.htm.]

——, J. C. Wyngaard, and J. M. Fritsch, 2003: Resolution requirements for the simulation of deep moist convection. *Mon. Wea. Rev.,* **131,** 2394–2416.

Chen, S. S., J. F. Price, W. Zhao, M. A. Donelan, and E. J. Walsh, 2007: The CBLAST-Hurricane Program and the next-generation fully coupled atmosphere–wave–ocean models for hurricane research and prediction. *Bull. Amer. Meteor. Soc.,* **88,** 311–317.

Corbosiero, K. L., J. Molinari, A. R. Aiyyer, and M. L. Black, 2006: The structure and evolution of Hurricane Elena (1985). Part II: Convective asymmetries and evidence for vortex Rossby waves. *Mon. Wea. Rev.,* **134,** 3073–3091.

Davis, C., and Coauthors, 2008: Prediction of landfalling hurricanes with the Advanced Hurricane WRF Model. *Mon. Wea. Rev.,* **136,** 1990–2005.

Dougherty, F., and S. Kimball, 2006: The sensitivity of hurricane simulations to the distribution of vertical levels. Preprints, *27th Conf. on Tropical Meteorology,* Monterey, CA, Amer. Meteor. Soc.

Emanuel, K. A., 1986: An air-sea interaction theory for tropical cyclone. Part I: Steady state maintenance. *J. Atmos. Sci.,* **43,** 585–604.

——, 1988: The maximum intensity of hurricanes. *J. Atmos. Sci.,* **45,** 1143–1155.

Fierro, A. O., M. S. Gilmore, E. R. Mansell, L. J. Wicker, and J. M. Straka, 2006: Electrification and lightning in an idealized boundary-crossing supercell simulation of 2 June 1995. *Mon. Wea. Rev.,* **134,** 3149–3172.

——, L. M. Leslie, E. R. Mansell, J. M. Straka, D. R. MacGorman, and C. Ziegler, 2007: A high resolution simulation of the microphysics and electrification in an idealized hurricane-like vortex. *Meteor. Atmos. Phys.,* **98,** 13–33, doi:10.1007/s00703-006-0237-0.

——, ——, ——, and ——, 2008: Numerical simulations of the electrification and microphysics of the weakly electrified 9th February 1993 TOGA COARE squall line, 2008: Comparisons with observations. *Mon. Wea. Rev.,* **136,** 364–379.

——, J. Simpson, M. A. LeMone, J. M. Straka, and B. F. Smull, 2009: On how hot towers fuel the Hadley cell: Observational and modeling study of line-organized convection in the equatorial trough from TOGA COARE. *J. Atmos. Sci.,* **66,** 2730–2746.

Gentry, M. S., and G. Lackmann, 2010: Sensitivity of simulated tropical cyclone structure and intensity to horizontal resolution. *Mon. Wea. Rev.,* in press.

Goerss, J. S., 2006: Prediction of tropical cyclone track forecast error for Hurricanes Katrina, Rita, and Wilma. Preprints, *27th Conf. on Hurricanes and Tropical Meteorology,* Monterey, CA, Amer. Meteor. Soc., 11A.1.

Gray, W. M., 1995: Tropical cyclones. Colorado State University Rep., World Meteorological Organization, 163 pp.

Heymsfield, A. J., A. Bansemer, S. L. Durden, R. L. Herman, and T. P. Bui, 2006: Ice microphysics observations in Hurricane Humberto: Comparison with non-hurricane-generated ice cloud layers. *J. Atmos. Sci.,* **63,** 288–308.

Hong, S. Y., J. Dudhia, and S. H. Chen, 2004: A revised approach to ice microphysical processes for the bulk parameterization of clouds and precipitation. *Mon. Wea. Rev.,* **132,** 103–120.

Houze, R. A., S. S. Chen, B. F. Smull, W.-C. Lee, and M. M. Bell, 2007: Hurricane intensity and eyewall replacement. *Science,* **315,** 1235–1239.

Janjic, Z. I., 1994: The step-mountain eta coordinate model: Further developments of the convection, viscous layer, and turbulence closure schemes. *Mon. Wea. Rev.,* **122,** 927–945.

Jorgensen, D. P., E. J. Zipser, and M. A. LeMone, 1985: Vertical motions in intense hurricanes. *J. Atmos. Sci.,* **42,** 839–856.

Kain, J. S., and J. M. Fritsch, 1993: Convective parameterization for mesoscale models: The Kain-Fritsch scheme. *The Representation of Cumulus Convection in Numerical Models, Meteor. Monogr.,* No. 24, Amer. Meteor. Soc., 165–170.

Kessler, E., 1969: *On the Distribution and Continuity of Water Substance in Atmospheric Circulations. Meteor. Monogr.,* No. 32, Amer. Meteor. Soc., 84 pp.

Kimball, S. K., and M. S. Mulekar, 2004: A 15-year climatology of North Atlantic tropical cyclones. Part I: Size parameters. *J. Climate,* **17,** 3555–3575.

Knabb, R. D., J. R. Rhome, and D. P. Brown, 2005: Tropical cyclone report: Hurricane Rita. Technical Rep., National Hurricane Center, National Oceanographic and Atmospheric Administration, 33 pp. [Available online at http://www.nhc.noaa.gov/2005atlan.shtml.]

Kossin, J. P., and M. D. Eastin, 2001: Two distinct regimes in the kinematic and thermodynamic structure of the hurricane eye and eyewall. *J. Atmos. Sci.,* **58,** 1079–1090.

——, and W. H. Schubert, 2001: Mesovortices, polygonal flow patterns, and rapid pressure falls in hurricane-like vortices. *J. Atmos. Sci.,* **58,** 2196–2209.

——, and ——, 2004: Mesovortices in Hurricane Isabel. *Bull. Amer. Meteor. Soc.,* **85,** 151–153.

Lee, W.-C., F. D. Marks, and R. E. Carbone, 1994: Velocity Track Display—A technique to extract real-time tropical cyclone circulations using a single airborne Doppler radar. *J. Atmos. Oceanic Technol.,* **11,** 337–356.

——, B. J.-D. Jou, P.-L. Chang, and F. D. Marks, 2000: Tropical cyclone kinematic structure retrieved from single Doppler radar observations. Part III: Evolution and structure of Typhoon Alex (1987). *Mon. Wea. Rev.,* **128,** 3982–4001.

LeMone, M. A., and E. J. Zipser, 1980: Cumulonimbus vertical velocity events in GATE. Part I: Diameter, intensity, and mass flux. *J. Atmos. Sci.,* **37,** 2444–2457.

Lin, Y.-L., R. D. Farley, and H. D. Orville, 1983: Bulk parameterization of the snow field in a cloud model. *J. Climate Appl. Meteor.,* **22,** 1065–1092.

Liu, Y., D. L. Zhang, and M. K. Yau, 1997: A multiscale numerical study of Hurricane Andrew (1992). Part I: Explicit simulation and verification. *Mon. Wea. Rev.,* **125,** 3073–3093.

——, ——, and ——, 1999: A multiscale numerical study of Hurricane Andrew (1992). Part II: Kinematics and inner-core structures. *Mon. Wea. Rev.,* **127,** 2597–2616.

Lonfat, M., F. D. Marks, and S. Chen, 2004: Precipitation distribution in tropical cyclones using the tropical rainfall measuring mission (TRMM) microwave imager: A global perspective. *Mon. Wea. Rev.,* **132,** 1645–1660.

Marks, F. D., 1985: Evolution of the structure of precipitation in Hurricane Allen (1980). *Mon. Wea. Rev.,* **113,** 909–930.

——, and R. A. Houze, 1987: Inner core structure of Hurricane Alicia from airborne Doppler radar observations. *J. Atmos. Sci.,* **44,** 1296–1317.

——, and L. K. Shay, 1998: Landfalling tropical cyclones: Forecast problems and associated research opportunities. *Bull. Amer. Meteor. Soc.,* **79,** 305–323.

——, R. A. Houze, and J. F. Gamache, 1992: Dual-aircraft investigation of the inner core of Hurricane Norbert. Part I: Kinematic structure. *J. Atmos. Sci.,* **49,** 919–942.

——, P. G. Black, M. T. Montgomery, and R. W. Burpee, 2008: Structure of the eye and eyewall of Hurricane Hugo (1989). *Mon. Wea. Rev.,* **136,** 1237–1259.

May, P. T., and D. K. Rajopadhyaya, 1996: Wind profiler observations of vertical motion and precipitation microphysics of a tropical squall line. *Mon. Wea. Rev.,* **124,** 621–633.

McFarquhar, G. M., and R. A. Black, 2004: Observations of particle size and phase in tropical cyclones: Implications for mesoscale modeling of microphysical processes. *J. Atmos. Sci.,* **61,** 422–439.

——, H. Zhang, G. Heymsfield, R. Hood, J. Dudhia, J. B. Halverson, and F. Marks, 2006: Factors affecting the evolution of Hurricane Erin (2001) and the distributions of hydrometeors: Role of microphysical processes. *J. Atmos. Sci.,* **63,** 127–150.

Mellor, G. L., and T. Yamada, 1982: Development of turbulence closure model for geophysical fluid problems. *Rev. Geophys. Space Phys.,* **20,** 851–875.

Michalakes, J., J. Dudhia, D. Gill, T. Henderson, J. Klemp, W. Skamarock, and W. Wang, 2005: The Weather Research and Forecast Model: Software architecture and performance. *Proceedings of the 11th ECMWF Workshop on High Performance Computing in Meteorology,* G. Mozdzynski, Ed., World Scientific, 156–168.

Molinari, J., and M. Dudek, 1992: Parameterization of convective precipitation in mesoscale numerical models: A critical review. *Mon. Wea. Rev.,* **120,** 326–344.

Montgomery, M. T., M. M. Bell, S. D. Aberson, and M. L. Black, 2006: Hurricane Isabel (2003): New insights into the physics of intense storms. Part I: Mean vortex structure and maximum intensity estimates. *Bull. Amer. Meteor. Soc.,* **87,** 1335–1347.

Nolan, D. S., Y. Moon, and D. P. Stern, 2007: Tropical cyclone intensification from asymmetric convection: Energetics and efficiency. *J. Atmos. Sci.,* **64,** 3377–3405.

Peng, M. S., B. F. Jeng, and R. T. Williams, 1999: A numerical study on tropical cyclone intensification. Part I: Beta effect and mean flow effect. *J. Atmos. Sci.,* **56,** 1404–1423.

Powell, M. D., 1990a: Boundary layer structure and dynamics in outer hurricane rainbands. Part I: Mesoscale rainfall and kinematic structure. *Mon. Wea. Rev.,* **118,** 891–917.

——, 1990b: Boundary layer structure and dynamics in outer hurricane rainbands. Part II: Downdraft modification and mixed layer recovery. *Mon. Wea. Rev.,* **118,** 918–938.

——, and T. A. Reinhold, 2007: Tropical cyclone destructive potential by integrated kinetic energy. *Bull. Amer. Meteor. Soc.,* **88,** 513–526.

Reasor, P. D., M. T. Montgomery, F. D. Marks, and J. F. Gamache, 2000: Low-wavenumber structure and evolution of the hurricane inner core observed by airborne dual-Doppler radar. *Mon. Wea. Rev.,* **128,** 1653–1680.

Rogers, R. F., S. Chen, J. Tenerelli, and H. Willoughby, 2003: A numerical study of the impact of vertical shear on the distribution of rainfall in Hurricane Bonnie (1998). *Mon. Wea. Rev.,* **131,** 1577–1599.

——, M. L. Black, S. S. Chen, and R. A. Black, 2007: An evaluation of microphysics fields from mesoscale model simulations of tropical cyclones. Part I: Comparisons with observations. *J. Atmos. Sci.,* **64,** 1811–1834.

Roux, F., and F. D. Marks, 1996: Extended Velocity Track Display (EVTD): An improved processing method for Doppler radar observations of tropical cyclones. *J. Atmos. Oceanic Technol.,* **13,** 875–899.

Rozoff, C. M., W. H. Schubert, B. D. McNoldy, and J. P. Kossin, 2006: Rapid filamentation zones in intense tropical cyclones. *J. Atmos. Sci.,* **63,** 325–340.

Rutledge, S. A., and P. V. Hobbs, 1983: The mesoscale and microscale structure and organization of clouds and precipitation in midlatitude cyclones. VIII: A model for the "seeder-feeder" process in warm-frontal rainbands. *J. Atmos. Sci.,* **40,** 1185–1206.

——, and ——, 1984: The mesoscale and microscale structure and organization of clouds and precipitation in midlatitude cyclones. XII: A diagnostic modeling study of precipitation development in narrow cold-frontal rainbands. *J. Atmos. Sci.,* **41,** 2949–2972.

Samsury, C. E., and E. J. Zipser, 1995: Secondary wind maxima in hurricanes: Airflow and relationship to rainbands. *Mon. Wea. Rev.,* **123,** 3502–3517.

Schubert, W. H., M. T. Montgomery, R. K. Taft, T. A. Guinn, S. R. Fulton, J. P. Kossin, and J. P. Edwards, 1999: Polygonal eyewalls, asymmetric eye contraction, and potential vorticity mixing in hurricanes. *J. Atmos. Sci.,* **56,** 1197–1223.

Shapiro, L. J., and J. L. Franklin, 1999: Potential vorticity asymmetries and tropical cyclone motion. *Mon. Wea. Rev.,* **127,** 124–131.

Simpson, R. H., 1974: The hurricane disaster potential scale. *Weatherwise,* **27,** 169–186.

Skamarock, W. C., J. B. Klemp, J. Dudhia, D. O. Gill, D. M. Barker, W. Wang, and J. G. Powers, 2005: A description of the Advanced Research WRF Version 2. NCAR Tech. Note, NCAR/TN-468+ST, 88 pp.

Stern, D. P., and D. S. Nolan, 2009: Reexamining the vertical structure of tangential winds in tropical cyclones: Observations and theory. *J. Atmos. Sci.,* in press.

Terwey, W. D., and M. T. Montgomery, 2008: Secondary eyewall formation in two idealized, full-physics modeled hurricanes. *J. Geophys. Res.,* **113,** D12112, doi:10.1029/2007JD008897.

Thompson, G., R. M. Rasmussen, and K. Manning, 2004: Explicit forecasts of winter precipitation using an improved bulk microphysics scheme. Part I: Description and sensitivity analysis. *Mon. Wea. Rev.,* **132,** 519–542.

Trier, S., W. Skamarock, M. LeMone, D. Parsons, and D. Jorgensen, 1996: Structure and evolution of the 22 February 1993 TOGA COARE squall Line: Numerical simulations. *J. Atmos. Sci.,* **53,** 2861–2886.

Wang, Y., 2002a: An explicit simulation of tropical cyclones with a triply nested movable mesh primitive equation model: TCM3. Part II: Model refinements and sensitivity to cloud microphysics parameterization. *Mon. Wea. Rev.,* **130,** 3022–3036.

——, 2002b: Vortex Rossby waves in a numerically simulated tropical cyclone. Part II: The role in tropical cyclone structure and intensity changes. *J. Atmos. Sci.,* **59,** 1239–1262.

Weisman, M. L., W. C. Skamarock, and J. B. Klemp, 1997: The resolution dependence of explicitly modeled convective systems. *Mon. Wea. Rev.,* **125,** 527–548.

Wiens, K. C., S. A. Rutledge, and S. A. Tessendorf, 2005: The 29 June 2000 Supercell observed during STEPS. Part II: Lightning and charge structure. *J. Atmos. Sci.,* **62,** 4151–4177.

Willoughby, H. E., 1990a: Temporal changes of the primary circulation in tropical cyclones. *J. Atmos. Sci.,* **47,** 242–264.

——, 1990b: Gradient balance in tropical cyclones. *J. Atmos. Sci.,* **47,** 265–274.

——, 1998: Tropical cyclone eye thermodynamics. *Mon. Wea. Rev.,* **126,** 3053–3067.

——, J. A. Clos, and M. G. Shoreibah, 1982: Concentric eyewalls, secondary wind maxima, and the evolution of the hurricane vortex. *J. Atmos. Sci.,* **39,** 395–411.

Wu, L., and S. A. Braun, 2004: Effects of environmentally induced asymmetries on hurricane intensity: A numerical study. *J. Atmos. Sci.,* **61,** 3065–3081.

Yang, B., Y. Wang, and B. Wang, 2007: The effect of internally generated inner-core asymmetries on tropical cyclone potential intensity. *J. Atmos. Sci.,* **64,** 1165–1188.

Yau, M. K., Y. Liu, D. L. Zhang, and Y. Chen, 2004: A multiscale numerical study of Hurricane Andrew (1992). Part VI: Small-scale inner-core structures and wind streaks. *Mon. Wea. Rev.,* **132,** 1410–1433.

Zhang, F., Y. Weng, Z. Meng, J. A. Sippel, and C. H. Bishop, 2009: Cloud-resolving hurricane initialization and prediction through assimilation of Doppler radar observations with an ensemble Kalman filter. *Mon. Wea. Rev.,* **137,** 2105–2125.

Zhu, H., and R. K. Smith, 2002: The importance of three physical processes in a three-dimensional tropical cyclone model. *J. Atmos. Sci.,* **59,** 1825–1840.

Zhu, T., and D. L. Zhang, 2006: Numerical simulation of Hurricane Bonnie (1998). Part II: Sensitivity to varying cloud microphysical processes. *J. Atmos. Sci.,* **63,** 109–126.

Zipser, E. J., 2003: Some views on ''hot towers'' after 50 years of tropical field programs and two years of TRMM data. *Cloud Systems, Hurricanes, and the Tropical Rainfall Measuring Mission (TRMM)—A Tribute to Dr. Joanne Simpson, Meteor. Monogr.,* No. 29, Amer. Meteor. Soc., 49–58.